Cross-Shelf Exchange in Prograde Antarctic Troughs Driven by Offshore Propagating Dense Water Eddies

Alan Gaul,[a,b] Weifeng (Gordon) Zhang,[c] Claudia Cenedese,[a]

[a] *Physical Oceanography Department, Woods Hole Oceanographic Institution, Woods Hole, MA 02543, United States*

[b] *MIT-WHOI Joint Program in Oceanography/Applied Ocean Science and Engineering, Cambridge and Woods Hole, MA, United States*

[c] *Applied Ocean Physics and Engineering Department, Woods Hole Oceanographic Institution, Woods Hole, MA 02543, United States*

Corresponding author: Alan Gaul, agaul@mit.edu

ABSTRACT: This study examines the link between near-bottom outflows of dense water formed in Antarctic coastal polynyas and onshore intrusions of Circumpolar Deep Water (CDW) through prograde troughs cutting across the continental shelf. Numerical simulations show that the dense water outflow is primarily in the form of cyclonic eddies. The trough serves as a topographic guide that organizes the offshore-moving dense water eddies into a chain pattern. The offshore migration speed of the dense water eddies is similar to the velocity of the dense water offshore flow in the trough, which scaling analysis finds to be proportional to the reduced gravity of the dense water and the slope of the trough side walls and to be inversely proportional to the Coriolis parameter. Our model simulations indicate that, as these cyclonic dense water eddies move across the trough mouth into the deep ocean, they entrain CDW from offshore and carry CDW clockwise along their periphery into the trough. Subsequent cyclonic dense water eddies then entrain the intruding CDW further toward the coast along the trough. This process of recurring onshore entrainment of CDW by a topographically constrained chain of offshore-flowing dense water eddies is consistent with topographic hotspots of onshore intrusion of CDW around Antarctica identified by other studies. It can bring CDW from offshore to close to the coast and thus impact the heat flux into Antarctic coastal regions, affecting interactions among ocean, sea ice, and ice shelves.

SIGNIFICANCE STATEMENT: Troughs cutting across the Antarctic continental shelf are a major conduit for the transport of dense shelf water from coastal formation regions to the shelf break. This study describes a process in which clockwise-spinning eddies moving offshore in prograde troughs successively entrain filaments of relatively warm Circumpolar Deep Water from offshore across the entire shelf and into the coastal region. This eddy-induced transport provides a new understanding of the shelf edge exchange process identified in previous studies and a mechanism for further onshore intrusion of the warm Circumpolar Deep Water over parts of the Antarctic shelf. The resultant onshore heat flux could potentially bring a substantial amount of heat from offshore into the coastal region and thus affect ice-ocean interactions through melting sea ice and ice shelves.

1. Introduction

Processes at the Antarctic coast affect the boundary conditions of both the Antarctic Ice Sheet and the abyssal ocean, and thus can greatly impact the climate system. Brine rejection during sea ice formation in coastal polynyas creates cold and saline Dense Shelf Water (DSW) that sinks to the shelf bottom and then flows offshore, forming Antarctic Bottom Water, the deepest water mass in the global ocean (Johnson 2008; Snow et al. 2016). Additionally, intrusions of relatively warm Circumpolar Deep Water (CDW) onto the continental shelf and then the coastal region can melt ice shelves (Jacobs et al. 1996) and reduce sea ice production (Guo et al. 2019).

Numerical simulations of polynya-sourced dense waters flowing offshore across gently sloped continental shelves show flows that are mostly in the form of eddies (Gawarkiewicz and Chapman 1995). Several factors, such as the Coriolis parameter, bottom slope, water depth, and ambient stratification, affect the dynamics of these dense water eddies – particularly their geometry, propagation speed, resting depth, and transport pathway (Gawarkiewicz 2000; Zhang and Cenedese 2014). While these studies of dense water outflow dynamics used idealized, along-shelf uniform topography, observations on the Antarctic shelf often show DSW flowing offshore in bathymetric troughs (Gordon et al. 2009). These troughs connect the shelf break directly to the Antarctic coast in the Antarctic Peninsula, the Adélie Coast, Prydz Bay, and the Bellingshausen, Amundsen, Weddell, and Ross Seas (Livingstone et al. 2012). They facilitate the offshore flow of dense water on the bottom via an along-isobath gravity current in the same direction as the phase propagation of coastal trapped waves (Chapman and Gawarkiewicz 1995; Wåhlin 2004; Kämpf 2005). As Chapman and Gawarkiewicz (1995) and Kämpf (2005) examined dense water offshore flows on the shelf in the initial transient state before dense water reaches the shelf break, the equilibrium-state dynamics of DSW flows in troughs on the shelf and its impact, upon reaching the shelf break, on onshore intrusions of offshore waters remains unexplored.

Studies have identified many mechanisms driving CDW intrusions onto the Antarctic continental shelf, such as along-isopycnal lateral eddy fluxes (Stewart et al. 2018), inertial overshoot of a shelf break jet across a curving shelf edge (Dinniman et al. 2003), and wind-driven coastal upwelling (Thoma et al. 2008). Some of these mechanisms are region-specific. For example, in the Bellingshausen Sea and West Antarctic Peninsula, the Antarctic Circumpolar Current impinges on the shelf edge, driving onshore CDW transport through bottom Ekman transport, shoaling of isopycnals, or flow instabilities (Klinck et al. 2004; Thoma et al. 2008; Zhang et al. 2011; Klinck and Dinniman 2010). In the Amundsen Sea, onshore flux of CDW through a submarine trough provides most of the heat required for ice shelf melting in the region (Walker et al. 2007). Multiple processes could induce such a localized CDW intrusion in a trough, including wind-forced Ekman pumping (Kim et al. 2017), interaction between along-shelf currents and irregular bathymetry (St-Laurent et al. 2013; Liu et al. 2022), an outflow of ice shelf meltwater (St-Laurent et al. 2013), and an outflow of DSW (Kämpf 2005; Morrison et al. 2020). A recent modeling study (Morrison et al. 2020) has shown that most CDW intrusions onto the Antarctic shelf happen in regions of strong DSW formation. As DSW flows offshore in a trough, the overlying sea surface height (SSH) lowers, creating a cross-trough (along-shelf) sea level gradient and driving onshore geostrophic flows of CDW. This mechanism can also be viewed as interfacial form stresses driving an eddy flux of CDW across the shelf break (Morrison et al. 2020). These studies focus on prominent retrograde troughs that are at least an order of magnitude wider than the typical baroclinic deformation radius over the Antarctic shelf and slope, which is 1.8 to 5.5 km (Morrison et al. 2020). A correlation between offshore dense water flow and onshore flow has also been observed at narrow irregular topography on the continental slope (Darelius et al. 2023). In narrower troughs, with widths of the same order of magnitude as the baroclinic deformation radius, baroclinic eddies might be confined by the topography. As a result, the flow dynamics in these narrower troughs may differ from those explored in previous studies.

As a step toward understanding the processes of trough-induced cross-shelf exchange on the Antarctic shelf, this study examines the dynamical process linking offshore flows of DSW with onshore flows of CDW in a narrow, prograde, submarine trough using idealized numerical simulations. The idealized trough in the model is qualitatively based on two troughs adjacent to the Enderby Land polynya in East Antarctica (Fig. 1d). Prograde troughs of similar geometry exist in other regions of the Antarctic shelf, such as a trough near Oates Land at 157°E, 68.85°S and the wider Hughes Trough in the Weddell shelf at 45°W, 74°S. The following section outlines the numerical setup used in this study. Section 3 presents results from a control simulation to give an overview of the general flow pattern of DSW outflow and CDW intrusion in a trough. Section 4 analyzes the impacts of trough geometry, stratification, and other parameters on dynamics of the exchange flow. Section 5 provides a general context for the model results. Section 6 summarizes key findings.

2. Methods

Numerical simulations presented in this study are based on the Regional Ocean Modeling System (ROMS), which integrates the hydrostatic, Boussinesq Navier-Stokes equations on an Arakawa C-grid (Haidvogel et al. 2008). Temperature variation is neglected for simplicity, as salinity has a leading impact on density for seawater around freezing temperatures. A salinity equation is integrated along with a linear equation of state with a haline contraction coefficient of 760 ppm kg g^{-1}. The rectangular model domain covers an area of 18,000 km × 900 km, which is much larger than the central study region of 300 km × 150 km where an idealized prograde trough is placed (Fig. 1c). The vast along-shelf span of the model domain is used along with boundary sponge layers to prevent long topographic waves from affecting the flow within and near the trough.

The shelf is oriented in the east-west direction with the coast along the southern boundary. The ambient bathymetry outside of the trough consists of a gently sloping continental shelf and a steep continental slope. Following that in Zhang and Lentz (2017), the seafloor depth, h_a, increases toward the north as

$$h_a = max\left[0, \frac{h_f - H_c}{l_f}\left(l_f + y\right)\right] + h_p\left(tanh\frac{y - y_p}{l_p} - 1\right) - h_f. \quad (1)$$

Here, the water depth at the coast has a default value of H_c = 500 m. The shelf depth scale h_f = 600 m and shelf width scale l_f = 100 km, such that the continental shelf has an offshore slope of 0.1%. The continental slope has a vertical scale of h_p = 750 m over a horizontal scale of l_p = 10 km, centered around the y coordinate y_p = 120km. The shelf break is defined to be at the 600 m isobath, which is 93 km offshore (north) of the coast. A Gaussian-shaped trough is added to the ambient shelf and slope, and the total water depth is given by

$$h = h_a - h_t e^{-(x-x_0)^2/W_c^2}. \tag{2}$$

Here, W_c is an along-shelf topographic length scale in the trough, and the trough width, $w_t = 4W_c$, is defined to encompass all areas with a topographic drop of at least 2% of the maximum trough depth h_t. To study a geometrically simple case, h_t is held constant with respect to y, resulting in a prograde trough. The implications of prograde versus retrograde troughs are discussed in section 3a. For the control simulations (Fig. 1a-c), these topographic parameters are chosen to approximate troughs in Enderby Land, East Antarctica (Fig. 1d).

The model has a horizontal grid resolution of 750 m x 750 m in a high resolution region that spans an area of 300 km x 225 km, a portion of which is shown in Fig. 1c. The model grid gradually coarsens to 105 km x 19.5 km toward the outer boundaries. Sponge regions are applied both at the east and west ends of the model domain. These regions are 7,500 km wide with horizontal viscosity and diffusivity increasing from zero within 2,000 km of the central study region to 100 m^2 s^{-1} at the boundary. Similarly, a 600 km wide sponge region is applied on the northern end of the model domain. The sponge regions damp long topographic waves generated by flow disturbances at the trough, preventing the waves from re-entering the study region after propagating through the periodic east-west boundaries. The model has 120 vertical terrain-following sigma levels (Shchepetkin and McWilliams 2005).

Periodic boundary conditions are used at the east and west boundaries. The coastal southern boundary is closed. Radiation boundary conditions for momentum and tracers (Orlanski 1976) and the Chapman boundary condition for sea surface height (Chapman 1985) are used on the northern boundary in the deep ocean. The Coriolis parameter, f, is uniform across the entire domain. A quadratic bottom friction parameterization with drag coefficient of 0.003 is used. The *k-kl* generic length scale turbulence closure scheme is used to parameterize vertical mixing.

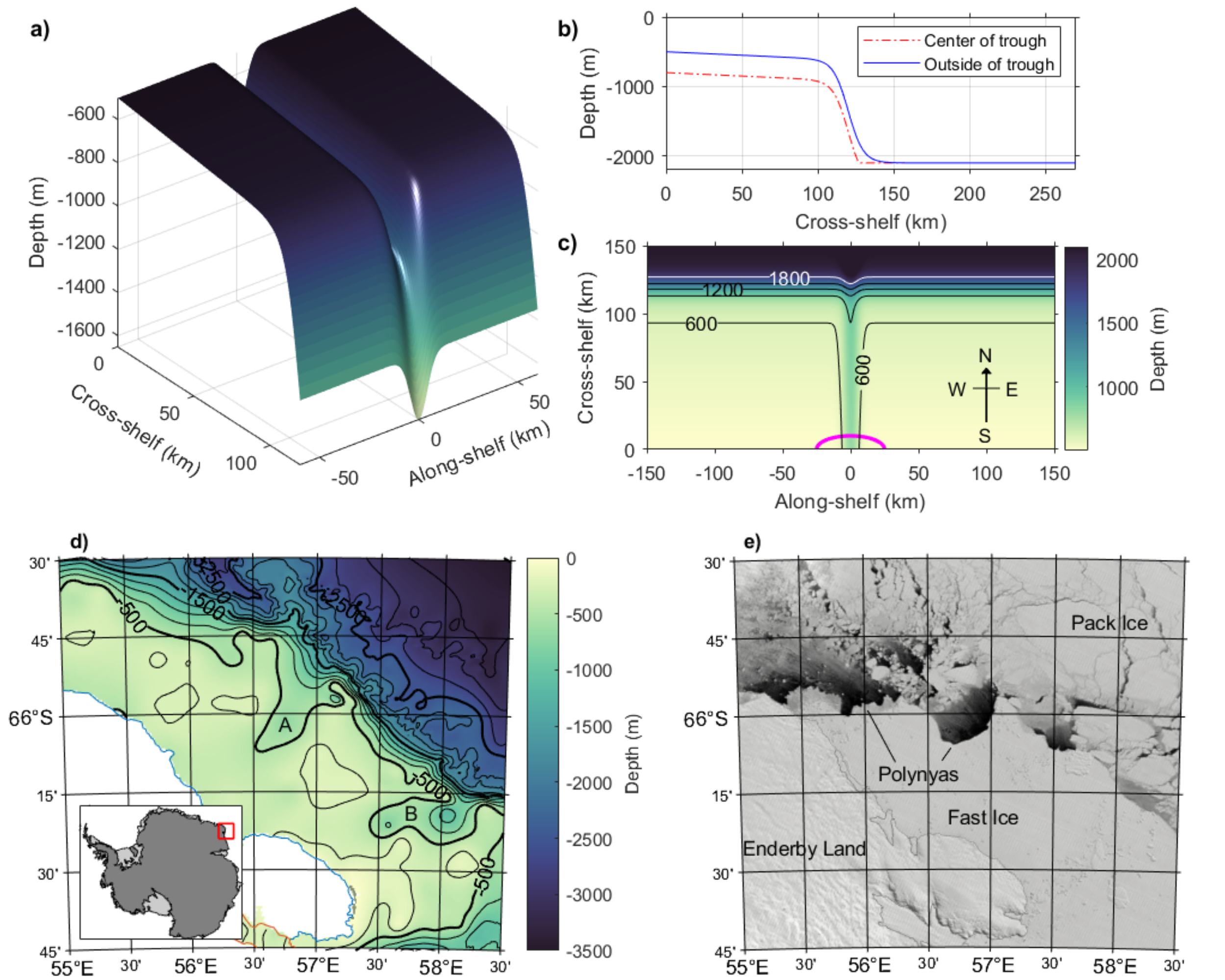

Fig. 1. (a-c) Model bathymetry for the control runs, from an (a) isometric, (b) side, and (c) birds-eye view. In panel (c), the magenta half-ellipse is the region of surface buoyancy forcing, and the black and white lines denote isobath contours. The coast is located on the southern boundary with a cross-shelf distance of zero km. While the full model domain extends 1,000 km offshore and 9,000 km east and west of the trough, only the area shown in panel (c) is analyzed in this study. d) RTopo-2 bathymetry near Enderby Land, East Antarctica. Idealized troughs used in this study are based upon troughs marked *A* and *B*. e) *Terra* MODIS satellite image of the Enderby polynya on 8 Sep. 2015.

All simulations start from rest with zero velocity and sea surface height. The control runs are initialized with an unstratified water column with a uniform salinity of 32. To simulate brine rejection in the polynya region, a constant evaporative freshwater flux, Q, is applied inside a coastal

TABLE 1. Parameters varied in sensitivity simulations, and their default values in control runs.

Sensitivity set	Varied parameter	Symbol	Units	Control value	Min. value	Max. value	# of runs
S-N_{ini}	Initial salinity stratification	$\Delta S/\Delta z$	psu km^{-1}	0	0	0.5	20
S-Q	Surface buoyancy flux	Q	10^{-7} $m^2 s^{-3}$	5.5	1.4	22.1	3
S-f	Coriolis parameter	f	10^{-4} s^{-1}	-1.37	-0.30	-2.74	4
S-H_c	Water depth at coast	H_c	m	500	100	700	5
S-h_t	Trough depth	h_t	m	300	100	800	7
S-w_t	Trough width	w_t	km	24	8	40	6
S-b	Elliptical forcing region minor axis	b	km	10	2	30	6

half-ellipse with an along-shelf major axis of a = 25 km and a cross-shelf minor axis of b (Fig. 1c). While past studies have allowed the buoyancy forcing to gradually decay outward to approximate a time-averaged fluctuating forcing region (i.e. Chapman 1999), in this study the decay region is omitted in order to measure dense water flow speeds more precisely. Five control simulations are run, each with randomly perturbed initial salinity at each surface grid cell in the forcing region (the salinity perturbations have a normal distribution centered around zero with a variance of 10^{-4}), to estimate the model uncertainty associated with nonlinearity of the circulation system.

Seven sets of sensitivity simulations with a trough (S-N_{ini}, S-Q, S-f, S-H_c, S-h_t, S-w_t, and S-b) are conducted to examine the dynamical impact of seven parameters: initial stratification $\Delta S/\Delta z$, surface evaporative flux Q, Coriolis parameter f, coastal water depth H_c, trough depth h_t, trough width w_t, and minor axis of buoyancy forcing region b. Each set consists of multiple simulations that vary only one parameter while holding all others equal to the control values. Table 1 shows values used in both the control runs and sensitivity simulations. Note that to vary the initial stratification, the bottom salinity is modified while holding the surface salinity fixed, such that salinity increases linearly with depth.

Two additional simulations, one without a trough and another with enhanced horizontal viscosity are run to test how the trough and eddies impact cross-shelf exchange. Both simulations have the same sensitivity parameter values as the control runs. The former has no trough. The latter has a trough, but its explicit horizontal viscosity is increased to 350 m^2 s^{-1} in the part of the central study region with y > 25 km to suppress eddies, while remaining at 0 m^2 s^{-1} in the coastal region to allow DSW formation in the forcing area. All other simulations have explicit horizontal viscosities of 0 m^2 s^{-1} everywhere. All simulations are run for 152 model days. A total of 56 simulations are presented in this work.

To quantify the influence of eddies on water mass exchange, we employ an eddy tracking algorithm from Faghmous et al. (2015). Cyclonic (anticyclonic) eddies are identified by finding the outermost closed contour containing a local maximum (minimum) in free surface height, and then these eddies are tracked from model days 80 to 152. Eddy kinetic energy (EKE) in the trough region from model days 80 to 150 is calculated following

$$EKE = \frac{(u-\overline{u})^2}{2} + \frac{(v-\overline{v})^2}{2}, \tag{3}$$

where $\bar{u}$ and $\bar{v}$ denote velocities averaged over a 70-day window, and u and v are snapshots of velocity recorded every two days.

To simulate the offshore dispersal of DSW and the onshore intrusions of CDW, two inert passive tracers are used. To represent the continuous generation of DSW at the polynya surface, the DSW passive tracer is continually set to a fixed concentration of 100% in the surface layer of the buoyancy forcing region. Along with the dense water, some of the DSW passive tracer sinks and propagates away from the source region. The CDW passive tracer is set to an initial concentration of 100% at every subsurface offshore location, which is defined as below 300 m depth and more than 7 km offshore of the shelf break (100 km offshore of the coast). Subject to advection and mixing, the CDW passive tracer evolves over time.

3. Results

a. General flow pattern

Results of Control Run 1 on Day 16 (Fig. 2) show a clear pattern of DSW, represented by a positive salinity anomaly, spreading outwards from the forcing region in both a westward-flowing current along the coast and an offshore-flowing bottom gravity current concentrated along the trough. Note that the offshore gravity current comprises of individual eddies translating offshore, as indicated by the localized maxima in vertically integrated salinity anomaly (Fig. 2). This pattern is consistent across all 5 control runs (not shown). The offshore speed of the nose of the DSW gravity current is discussed in section 4a. Similar to those in previous studies (e.g.

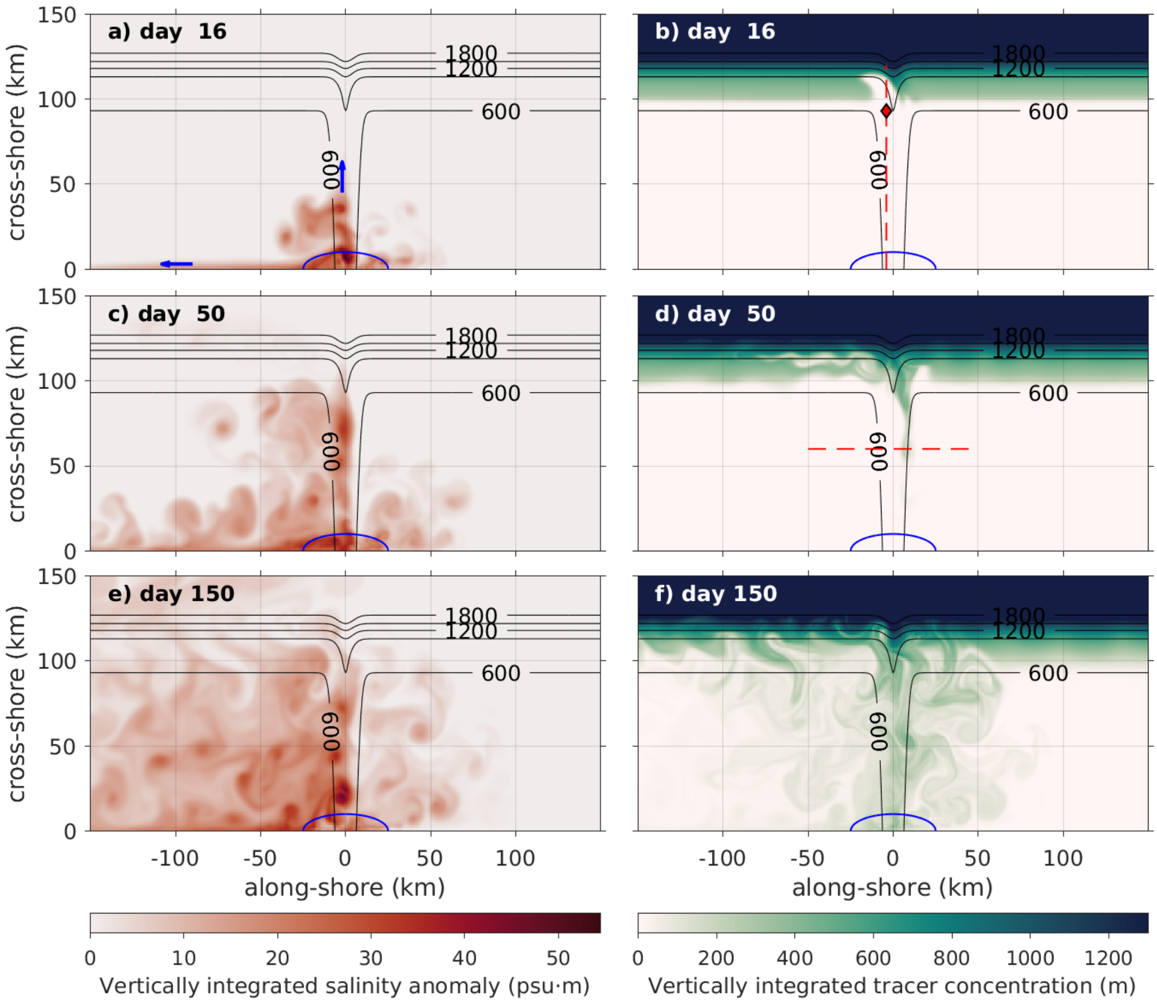

FIG. 2. Vertically integrated (a, c, e) salinity anomaly and (b, d, f) CDW tracer from Control Run 1 at model days 16, 50, and 150. Black lines denote isobath contours. Blue half-ellipse shows the region of surface buoyancy forcing. Note the color range for b, d, and f is saturated to highlight the CDW that has intruded onto the shelf. The blue arrows in (a) denote primary westward and offshore flow directions. The red dashed lines in (d) and (b) indicate the locations of the transects shown in Figs. 4 and 12, respectively. The red diamond in (b) is the location of the velocity spectrum shown in Fig. 15. Videos of these variables are provided in the supplementary material.

Chapman and Gawarkiewicz 1995; Zhang and Cenedese 2014), these DSW eddies are cyclonic (clockwise-rotating) vortices that likely form through baroclinic instability and conservation of potential vorticity (PV). Detailed dynamics of DSW eddy formation are discussed in section 4a.

By Day 50, the furthest offshore dense water eddy has reached the trough mouth at the shelf break and begun cascading down the western continental slope. Meanwhile, several offshore flowing dense water eddies have lined up in the trough, flowing along the western side of the trough with shallower isobaths on their left. This orientation is consistent with the translation of isolated dense water eddies on a sloping bottom, which is in the same direction as the propagation of topographic waves (Nof 1983). The along-isobath propagation of the eddies is associated with a cross-isobath (cross-trough, in this case) momentum balance between a down-slope gravitational force and an up-slope Coriolis force (Nof 1983). By the end of the control runs, on average, the volume of DSW that has moved offshore of the shelf break in the form of eddies is about two times the DSW volume that has propogated westward along the coast on the shelf. Therefore, the eddy-induced offshore transport in the trough represents a major transport pathway of the modeled DSW.

The model results also show that as DSW flows offshore in the trough, CDW intrudes into the trough and then onto the shelf. On Day 50, a filament of CDW over 50 km long intrudes into the trough, hugging the eastern flank of the DSW eddy (Fig. 2d). By Day 150, CDW has reached the coast and is mixed across the trough and continental shelf (Fig. 2f). The highest concentrations of CDW are over the eastern slope of the trough and the shelf to its east, while CDW on the shelf to the west of the trough is more spread out and diluted.

Time series of modeled cross-shelf fluxes can be divided into three phases. Before Day 20, DSW has not yet reached the shelf-break, so the cross-shelf salinity anomaly flux across the shelf-break is zero (Fig. 3a). After Day 20, the flux grows linearly as the model continues to spin up. Finally, by Day 80, the flux levels off as the system reaches equilibrium with no statistically significant trends. The shelf-break salinity anomaly flux at the trough, averaged over Days 80-152 and over the control runs, is 6×10^3 psu m^3 s^{-1}. The standard deviations of salinity anomaly flux in Days 80-152, averaged across the control runs, is 5×10^3 psu m^3 s^{-1}. The eddy-driven variability in salinity anomaly flux thus has the same magnitude as the mean flux. Similarly, the cross-shelf flux of CDW tracer across a transect at 60 km offshore has comparable phases and reaches equilibrium by Day 80 (Fig. 3b), with an average equilibrium flux of -1.4×10^5 m^3 s^{-1} and an average standard deviation of 1.2×10^5 m^3 s^{-1}. Furthermore, the equilibrium CDW tracer flux in Control Run 1 can be decomposed into a mean flux of $\overline{v}\overline{\frac{\Delta C}{\Delta y}} = -24$ m^3 s^{-1} and an eddy flux of $\overline{v'\frac{\Delta C'}{\Delta y}} = -1.3\times10^5$ m^3 s^{-1}, where the overbars denote average over Days 80-152 and C is the volume-integrated concentration

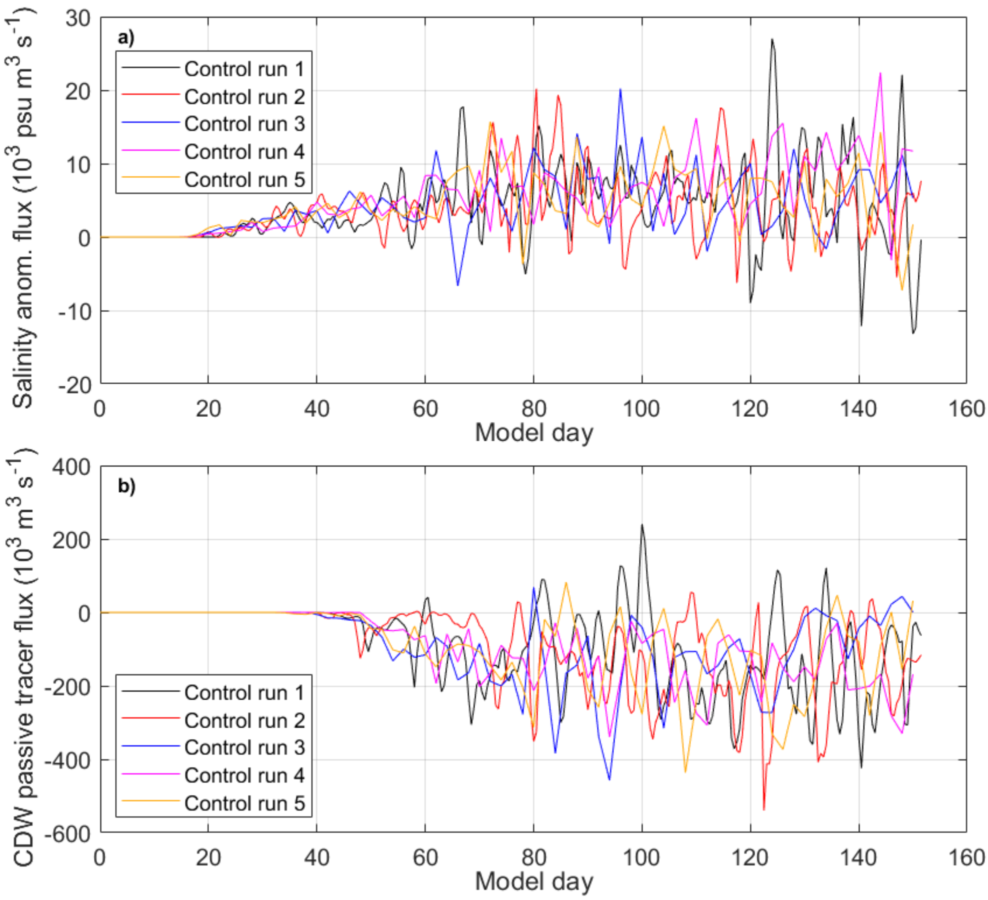

FIG. 3. Timeseries of cross-shelf flux of (a) salinity anomaly across the blue line in Fig. 10d, summed over the entire water column, and (b) CDW tracer across a similar line at 60 km offshore, for each control run. Note negative flux corresponds to onshore flow.

of CDW tracer. The relatively large eddy flux indicates that the modeled cross-shelf CDW flux is episodic and likely driven by eddies.

An along-shelf transect across the trough at $y = 60$ km shows that the core of the time-averaged offshore current of DSW is bottom-intensified and concentrated on the western side of the trough (Fig. 4b). The time-averaged flow on the eastern side of the trough is onshore and largely barotropic, similar to the trough-steered CDW inflow modeled by Morrison et al. (2020). Our model shows a localized SSH lowering (raising) over the western (eastern) slope of the trough (Fig. 4a), similar to the model result in Morrison et al. (2020). The dynamics causing this SSH gradient

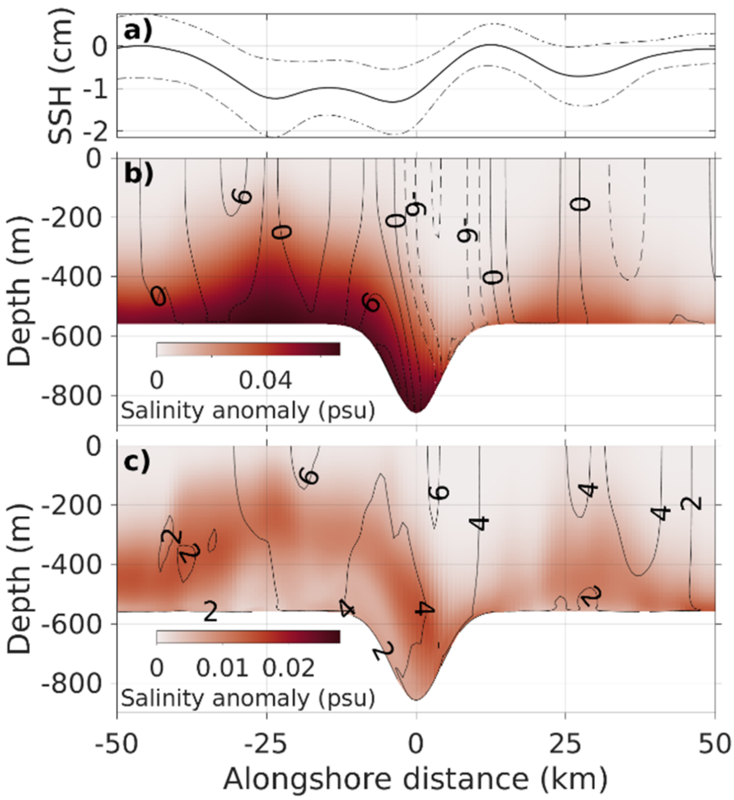

FIG. 4. (a) Sea surface height along an along-shelf transect at 60 km offshore of the coast (dashed line in Fig. 2d) from Control Run 1, averaged over days 100-150. The dash-dotted line shows ± one standard deviation. (b) Vertical section of salinity anomaly (color) and cross-shelf velocity in cm s^{-1} (contours) along the transect, also averaged over days 100-150. Positive velocities (solid lines) are directed offshore. (c) Vertical section of standard deviation of salinity anomaly (color) and cross-shelf velocity (contours) along the transect.

over the eastern slope of the trough (Fig. 4a) will be discussed in section 4b. This onshore flow on the eastern slope of the trough has a high variability due to its eddy-dominated nature (Fig. 4c).

b. CDW intrusion event case study

Intrusion of CDW into the trough and then onto the continental shelf in Control Run 1 appears to be associated with the offshore-moving DSW eddies in the trough (Fig. 2c-d). Before explaining the dynamics driving this intrusion (section 4b), we here examine the detailed behavior of DSW and CDW near the shelf break and in the trough in Control Run 1 to qualitatively illustrate the cross-shelf exchange of these water masses. Because the pattern of CDW intrusion at the beginning of the simulation is clearer, with less background variation than later in the simulation, we here use the initial CDW intrusion to illustrate the process. However, the process of CDW intrusion remains qualitatively similar later in the simulations.

On Day 30, a filament of DSW extends northwestward from the trough onto the continental slope (Fig. 5a). This DSW gravity current flows in the same direction as coastal trapped waves. A cyclone, C1, is visible in the trough at 50 km offshore as a local maximum in salinity anomaly and a perturbation in PV in the overlying layer of ambient water. CDW has not yet intruded onshore of the shelf break (Fig. 6a). By Day 47.5, DSW cyclone C1 has moved 20 km closer to the shelf break and intensified into an eddy with closed contours of PV (Fig. 5b). A second eddy, C2, follows C1 through the trough. Meanwhile, a filament of CDW flows shoreward on the eastern flanks of both eddies (Fig. 6b). The onshore intruding CDW is concentrated on the eastern slope of the trough. By Day 53, the leading DSW eddy, C1, reaches the trough mouth at the shelf break (Fig. 5c), C2 has merged into C1, and another DSW cyclone, C3, has formed inside the trough at 40 km offshore. Meanwhile, the CDW filament has extended further southward along the eastern slope of the trough, reaching the eastern flank of C3 (Fig. 6c). Close examination of the model result shows that the nose of the CDW filament has already reached the coastal buoyancy forcing region by Day 53. However, due to mixing, CDW passive tracer concentration in the nose has been diluted, and its signal is faint (Fig. 6c). By Day 57, the trailing DSW cyclone, C3, has moved farther northward, reaching 60 km offshore (Fig. 5d), and the CDW filament has intruded farther onshore, closer to the coast. Meanwhile, some CDW has flowed westward across the trough along the southern flank of Eddy C1 at 75 km offshore. These results suggest that the initial shoreward intrusion of the CDW filament into the trough is associated with the successive offshore-moving DSW eddies in the trough. Note that, at any time, between 1 and 3 DSW eddies reside within the trough. After this initial stage, CDW that has intruded into the trough mixes with ambient waters and propagates onto the neighboring continental shelf (Fig. 2f).

4. Dynamics

a. Eddy formation and propagation

Examination of the model results indicates that eddies of DSW flowing offshore along the trough are coupled with cyclonic eddies in the overlying ambient fluid. Some of the DSW eddies form by

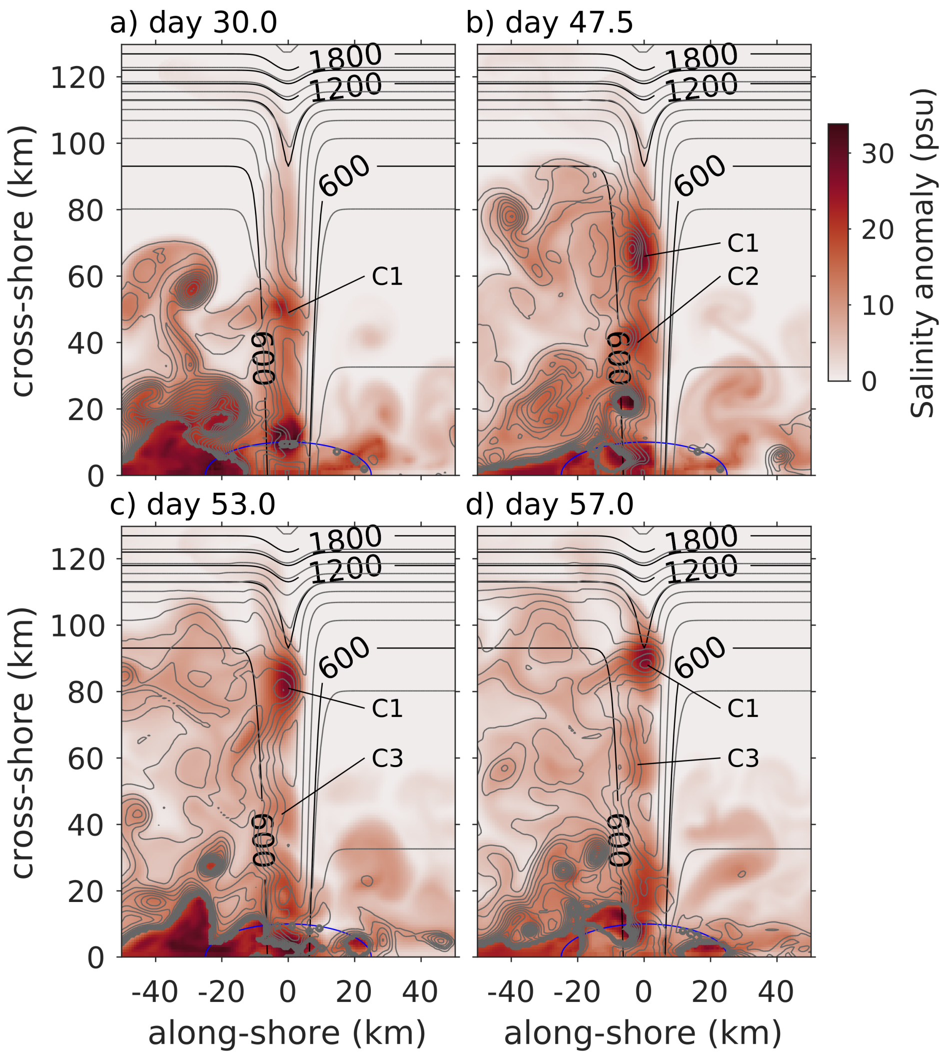

FIG. 5. Salinity anomaly vertically integrated over the entire water column (color) and potential vorticity of the overlying ambient water layer (grey contours with intervals of 2×10^{-8} m^{-1} s^{-1}) from Control Run 1, at model Days (a) 30, (b) 47.5, (c) 53, and (d) 57. Black lines show isobath contours. The blue half-ellipse shows the region of surface buoyancy forcing. Potential vorticity is only shown when the ambient layer is thicker than 200 meters. The ambient layer depth is defined as the depth at which the salinity anomaly exceeds 0.045 psu.

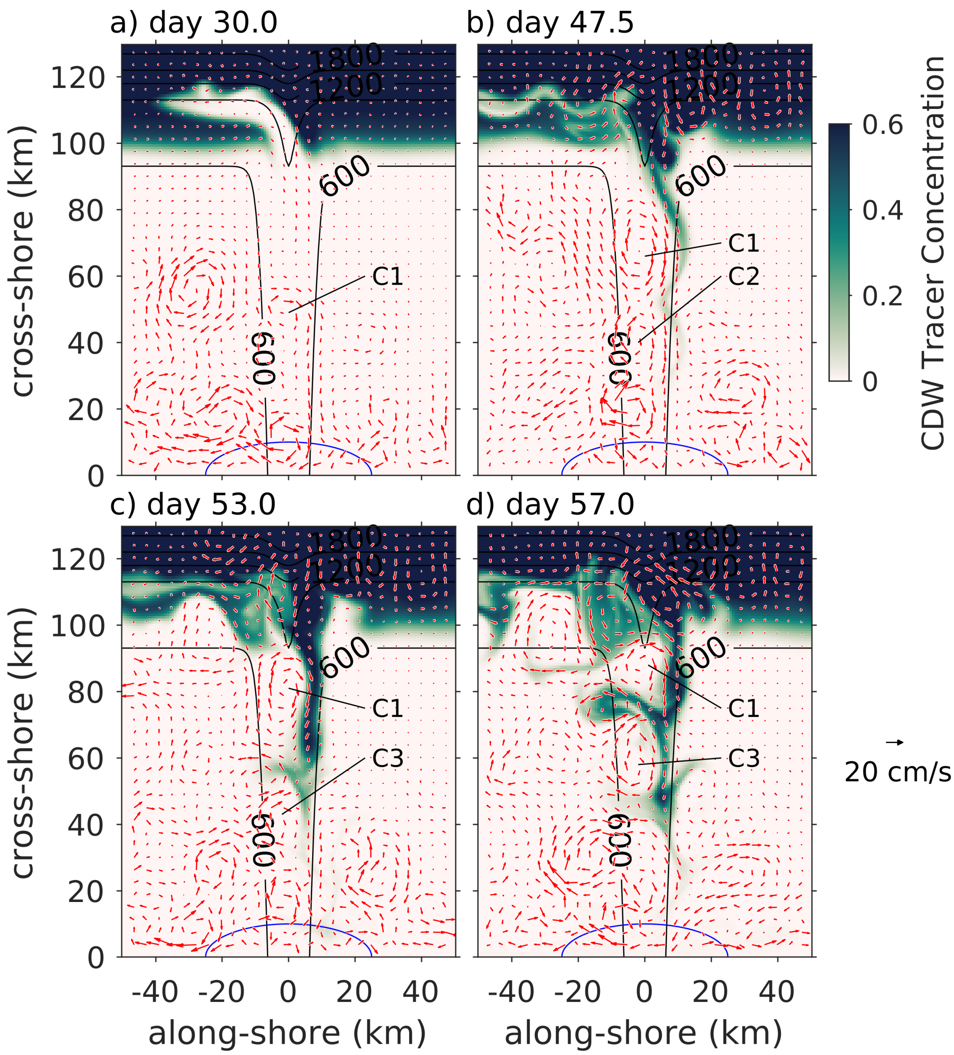

269 FIG. 6. Vertically averaged CDW passive tracer concentration (color) and velocity (arrows) from Control Run
270 1, at model days (a) 30, (b) 47.5, (c) 53, and (d) 57. Black lines show isobath contours. The blue half-ellipse
271 shows the region of surface buoyancy forcing. Note the color range is saturated to highlight structure at small
272 concentrations.

pinching off from a baroclinically unstable circum-polynya current that is generated through thermal wind balance on the periphery of the polynya (Gawarkiewicz and Chapman 1995). Initially, these features are nonlinear Topographic Vorticity Wave (TVW) solitons associated with open contours of PV in the overlying ambient water layer (Fig. 5a, c). As these TVW solitons descend along the deepening trough, they bring along a Taylor column of overlying ambient water, consistent with Swaters (1998) and Zhang and Cenedese (2014). The ambient water stretches vertically and, to conserve PV, develops positive relative vorticity, spinning cyclonically (clockwise). Similar eddy formation is observed in laboratory studies of dense water outflows over continental slopes (Lane-Serff and Baines 2000; Cenedese et al. 2004). Correspondingly, the depth-averaged flow field in Control Run 1 is dominated by cyclonic rotation (Fig. 6). Some of the TVW solitons intensify over time due to continued vortex stretching as they move further along the trough into deeper waters, such that the entire water column (including the bottom DSW layer) spins faster cyclonically, forming mesoscale eddies with closed contours of PV (Fig. 5b, d). For brevity, we refer to both TVW solitons and eddies as eddies in this paper.

We now compare eddy propagation pathways in the simulations with and without a trough. In the simulation without a trough, eddies are scattered over the continental shelf, with no consistent spatial pattern (Fig. 7a-b). The average cross-shelf translational velocity of these eddies is not significantly different from zero (0 ± 2 cm s^{-1}). Eddy-driven advection is the main, albeit slow, mechanism by which DSW flows offshore and CDW moves shoreward. When a trough is added, cyclonic eddies propagate offshore along isobath contours on the western side of the trough (red tracks in Fig. 7c). These cyclonic DSW eddies in the trough move offshore at speeds of 4 ± 4 cm s^{-1} in Control Run 1, when averaging over all cyclonic eddies in the trough for model days 80 to 150. The corresponding speed in Control Run 2 is 6 ± 4 cm s^{-1}, and it is similar in other control runs (not shown). In Control Run 1, a substantial portion of the anticyclonic eddies propagate onshore just east of the trough (blue tracks in Fig. 7d). These anticyclonic eddies have CDW cores (see section 4b). Both DSW and CDW eddies propagate in the same direction that a coastal-trapped wave propagates in the southern hemisphere – along-isobaths with shallow water to the left. The motion of individual cyclonic DSW eddies collectively forms a DSW offshore current along the western slope of the trough. The average speed of the DSW eddy propagation offshore in the

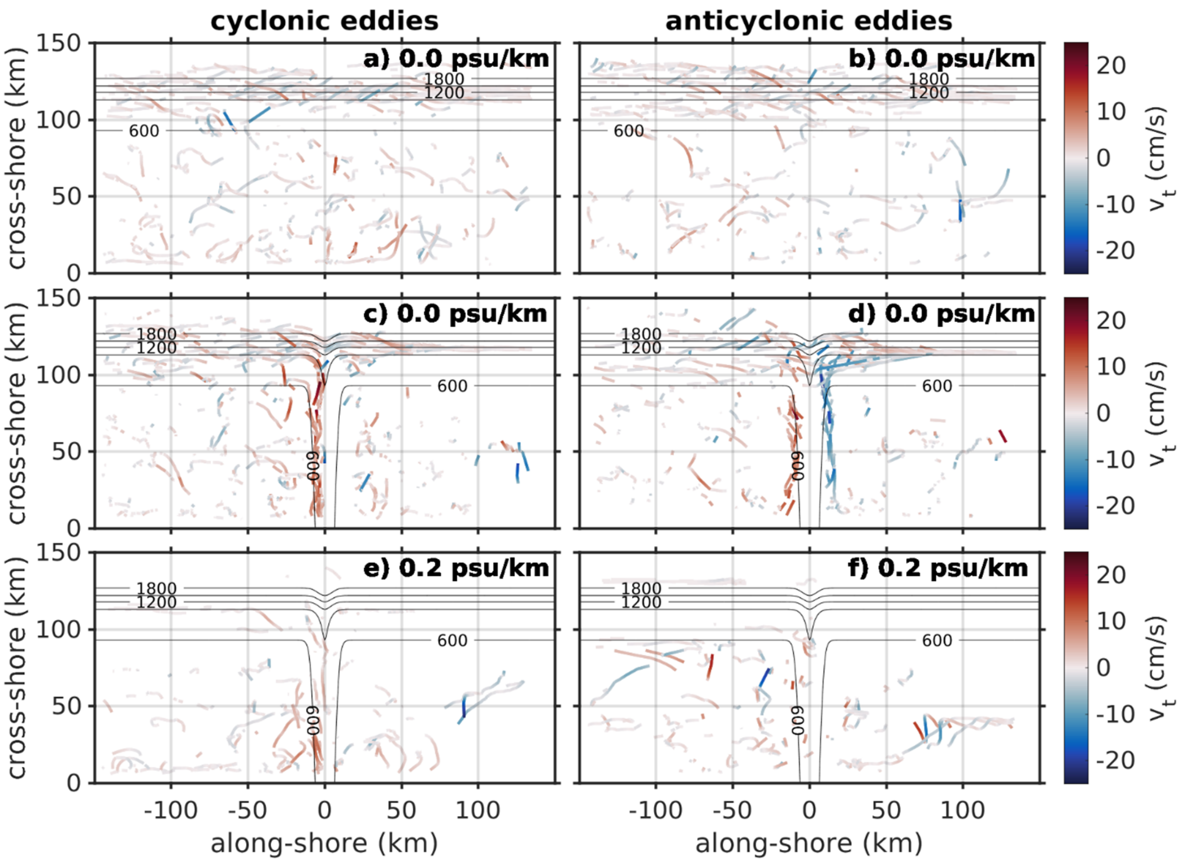

FIG. 7. Tracks of (a, c, e) cyclonic and (b, d, f) anticyclonic eddies for (a-b) an initially unstratified simulation with no trough, (c-d) an initially unstratified Control Run 1 with a trough, and (e-f) a simulation with a trough and an initial stratification of 0.2 psu km^{-1}. The color of the tracks shows the cross-shelf eddy translation speed, with red meaning the eddy moves offshore (northward).

trough is comparable to the speed of a dense water gravity current on a sloping bottom, as shown by a scaling analysis described below.

To obtain a scaling for the mean velocity of the DSW flowing offshore along the trough, we consider the flow of the time-averaged eddy field, rather than the propagation of individual eddies. Zhang and Cenedese (2014), using a similar approach, found the speed of a gravity current along a sloping bottom in an unstratified ambient fluid to be dictated by a balance between the down-slope baroclinic pressure gradient force and the up-slope Coriolis force, consistent with the momentum balance of an isolated dense water eddy on a sloping bottom (Nof 1983). Equation 8 of Zhang and

Cenedese (2014) gives the speed of the gravity current,

$$V = c\frac{g'\alpha}{|f|}, \tag{4}$$

where the reduced gravity of the dense water relative to the ambient water is written as

$$g' \approx \frac{C_c^{\frac{4}{3}} b^{\frac{2}{3}}}{2^{\frac{1}{3}}} \frac{Q^{\frac{2}{3}}}{H_c}. \tag{5}$$

Here, c is a constant given by the ratio of the gravity current thickness to the water depth, α is the bottom slope, and C_c depends on the forcing region geometry. In this study, the bottom slope in the trough in the cross-isobath (along-shelf) direction is $\alpha = 2h_t/w_t$. Equations 4 and 5 can thus be combined to give

$$V = Cb^{\frac{2}{3}} \frac{Q^{\frac{2}{3}} h_t}{H_c w_t |f|}, \tag{6}$$

where

$$C \equiv 2^{\frac{2}{3}} c C_c^{\frac{4}{3}}. \tag{7}$$

Equation 6 indicates that the along-isobath gravity current speed increases with h_t, Q, and b, and decreases with w_t, H_c, and $|f|$.

This analytical result is compared to the modeled offshore flow speed, V, in the trough for different sensitivity parameters (i.e., h_t, w_t, Q, H_c, b, and f, see Fig 8). The modeled V is defined as the mean offshore speed of the nose of the DSW flow in the trough, which is obtained from the slope of a linear regression of the offshore position of the nose versus time. The nose is defined as the offshore-most point in an along-trough transect at which the DSW concentration is greater than 0.1%. Averaged over the control runs, the speed of the nose of the DSW gravity current flowing down the trough is 5.5 ± 0.7 cm s^{-1}. In general, the sensitivity simulations give the same trends of dependence of V on the parameters as described by Equation 6. In particular, modeled V increases with increasing trough depth and decreasing trough width, which is consistent with V increasing with trough slope, α. Modeled V also increases with buoyancy flux, Q, and polynya width, b, representing the positive relation of V with the reduced gravity, g'. When Q or b increase, more salt is added to the water column, which increases g'. Conversely, modeled V decreases with increasing coastal water depth, H_c, as the dense water is diluted more as it sinks further. Finally, modeled V decreases with increasing magnitude of the Coriolis parameter, $|f|$.

A scatter plot of all modeled vs. scaled V shows a collapse of the comparison around a straight line (Fig. 9). A least-squares fit of the scatter comparison gives a value of the coefficient $C \approx 1.7$. Applying this value to Equation 6 provides the scaled dependencies of V on the sensitivity parameters (lines in Fig. 8). These scalings are consistent with those modeled by the sensitivity simulations. The only parameter with a clear discrepancy in the comparison is the buoyancy flux, Q (Fig. 8c). The simulations have a stronger dependence of V on Q than predicted by the scaling. This discrepancy was also seen in Zhang and Cenedese (2014) and may result from parameterized vertical mixing of dense water in the numerical model being inconsistent with the instant mixing over the entire water column assumed in the scaling analysis (Chapman and Gawarkiewicz 1997).

The close agreement of simulated flow speeds to the analytical scaling shows that, to first order, the dynamics of the modeled DSW gravity current in the trough are consistent with that of a gravity current over a uniformly sloping bottom as described in the scaling analysis. That is, despite the geometric constraint of the trough, the northward DSW outflow in the trough is mostly in a balance between the downslope (cross-trough, eastward) gravity force and the upslope (westward) Coriolis force. Note that the deformation radius of the DSW gravity current here is on the order of 2 km, which is smaller than the trough width (8 to 40 km). It is likely that this dynamical balance will change when the trough width becomes smaller than the deformation radius.

b. Eddy-induced CDW intrusion

The simulations show that CDW intrusion into the trough can be induced by successive cyclonic DSW eddies moving offshore along and then exiting the trough. As mentioned in section 3b, soon after the first cyclonic DSW eddy, C1, reaches the shelf break (Fig. 5), a CDW filament begins to intrude on the eastern side of the trough (Fig. 6). The close timing of these events is not a coincidence; DSW eddies actively pull CDW shoreward. The diameter of the DSW eddies is of similar magnitude to the trough width, and these eddies are centered on the western slope of the trough. As a result, the eastern portion of the cyclonic DSW eddies, which has a shoreward flow, is located on the eastern slope of the trough. Note that the offshore migration speed of the DSW eddies is 6 ± 4 cm s^{-1} in Control Run 2. This is weaker than the azimuthal speed of the eddies,

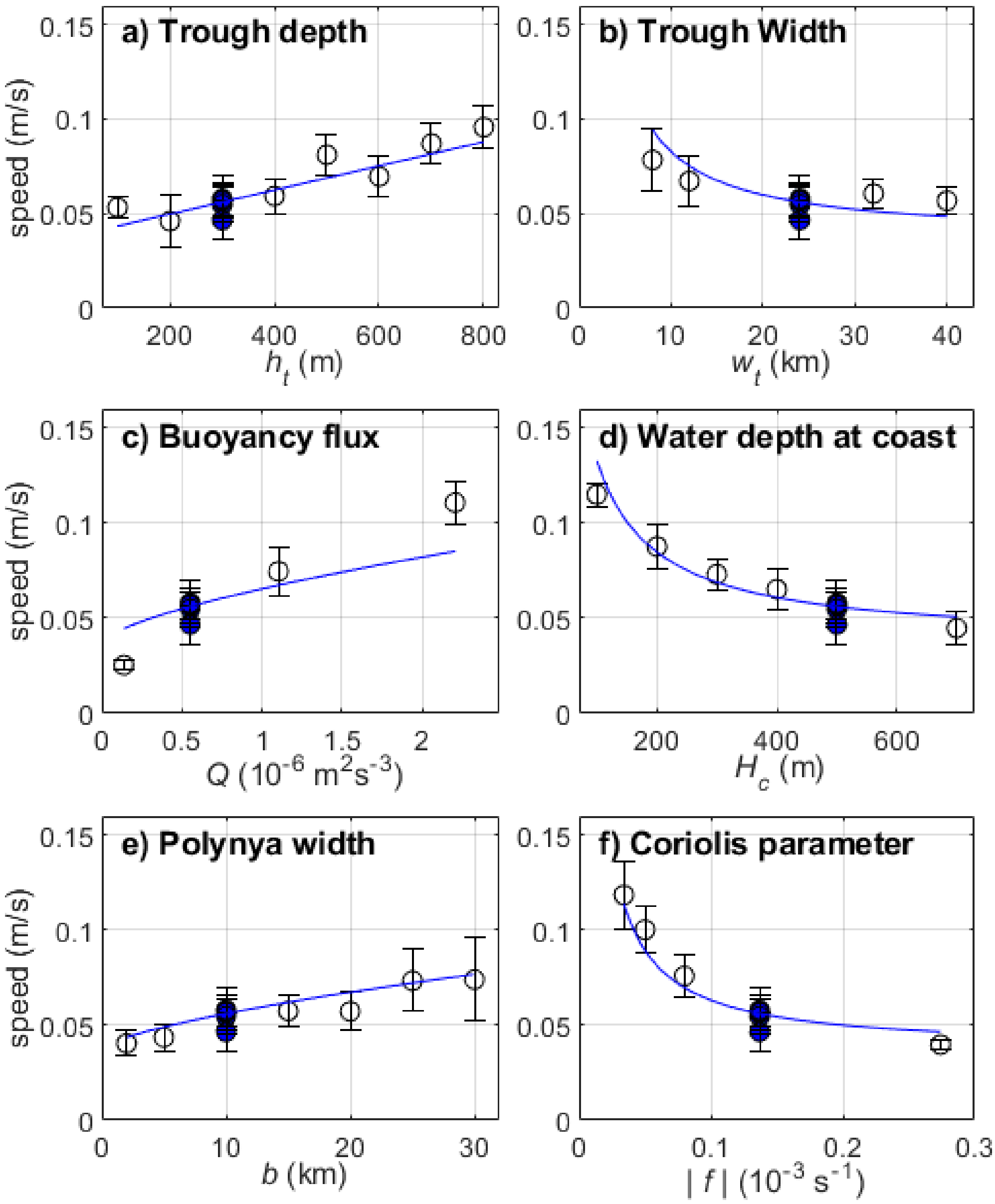

FIG. 8. Modeled DSW current speed versus (a) trough depth h_t, (b) trough width w_t, (c) surface buoyancy flux Q, (d) water depth at the coast H_c, (e) cross-shelf width of the buoyancy forcing region b, and (f) absolute value of Coriolis parameter $|f|$. The filled circles represent control simulations. The error bars show the standard deviations of the modeled speeds. The blue lines are the scaled speed from Equation 6 with the coefficient $C = 1.7$ as determined from the least-squared fit in Fig. 9.

which Fig. 6 shows to have a range of roughly 10-15 cm s^{-1}. Therefore, the Eulerian velocity of the water on the eastern side of the eddy is shoreward even though the eddies migrate offshore

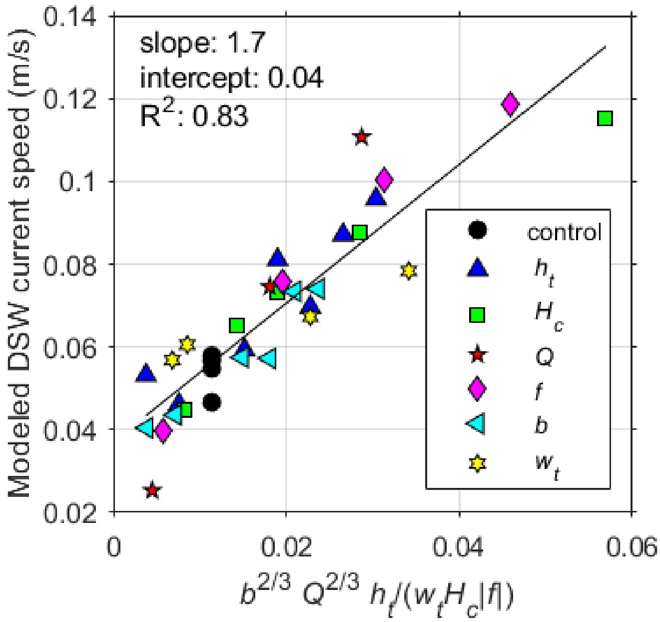

FIG. 9. Speeds of modeled DSW currents in the trough versus scaled gravity current speeds from Equation 6. The symbols show the corresponding parameters that have been varied in each simulation. The least squares fit is shown as a solid line, along with the slope, y-intercept, and R^2 value.

in the trough, allowing eddy C1 to entrain CDW shoreward when it reaches the shelf break. The entrained CDW forms a filament that snakes shoreward over the eastern slope of the trough (Fig. 6). This process is similar to mesoscale Gulf Stream warm core rings pulling shelf water offshore into submesoscale shelf water filaments along the outskirt of the rings (Garfield III and Evans 1987; Cherian and Brink 2016; Zhang et al. 2023). On Day 47.5, the DSW filament formed by eddy C1 in Control Run 1 extends over 50 km shoreward in the trough (Fig. 6b). Through the same mechanism, subsequent eddies C2 and C3 pull the CDW filament further shoreward in the trough (Fig. 6b-d). In this way, a chain of eddies moves CDW towards the coast in a pattern similar to a bucket brigade, which is a line of people passing buckets of water towards a fire.

For DSW eddies to create a significant CDW intrusion onto the shelf, multiple slow-moving DSW eddies must be present along a cross-shelf pathway, which requires a topographic guide such as a trough. A single eddy can only pull CDW onshore a maximum distance equal to the eddy diameter – a few tens of kilometers. Without a subsequent eddy streaming the CDW further shoreward, the intruding CDW would remain in the outer-shelf region instead of reaching the coast about 100 km further onshore. The simulation without a trough confirms this. In this simulation, cyclonic DSW eddies have inconsistent paths and rarely reach the shelf break (Fig. 7a). Correspondingly, the volume of CDW that intrudes to within 25 km of the coast by Day 150 is only 5.8×10^{10} m^3. In the control runs with troughs, however, the corresponding volume of CDW increases to $38.3 \times 10^{10} \pm 1.8 \times 10^{10}$ m^3. Adding a trough increases the onshore CDW flux. Thus, the trough provides a topographic guide along which DSW eddies propagate in a chain, successively streaming CDW onshore to the coastal region.

The preceding analysis focuses on the initial development of the CDW onshore intrusion into the trough. Examining the simulation at later stages, when the flow field is more complex, suggests that offshore moving DSW eddies continue to drive CDW intrusions. This can be seen in composite plots of relative vorticity at 580 m depth and vertically-integrated salinity anomaly made by averaging over times of anomalously large onshore CDW fluxes across the shelf break (Fig. 10). On average, large onshore CDW flux occurs when a cyclonic DSW eddy, as indicated by a patch of negative relative vorticity (cyclone) and a local maximum in salinity anomaly, reaches the trough mouth region about 90-95 km offshore. Meanwhile, a patch of positive relative vorticity (anticyclone; Fig. 10c) with enhanced CDW tracer concentration (Fig. 10e) forms to the east of the DSW eddy (Fig. 10c). This is consistent with conservation of potential vorticity as CDW is brought from offshore waters into the shallower trough, compressing the water column. Presumably through the same mechanism, the onshore propagation of the anticyclones along the eastern slope of the trough (Fig. 6d) up the trough into shallower water maintains their positive relative vorticity. Note that cross-correlation of the time series of onshore CDW flux and offshore salinity anomaly flux indicates that peak CDW onshore fluxes usually lead peak offshore salinity anomaly flux by 1-2 days. This offset occurs because a DSW cyclone can start inducing onshore CDW flux when its northern edge first reaches the trough mouth (blue line in Fig. 10d), while its main body remains onshore of the trough mouth. This is consistent with the DSW cyclone being slightly onshore of the CDW anticyclone at the trough mouth region during the times of peak onshore CDW flux (Fig. 10c).

To further confirm the role of eddies in driving the water mass exchange, we compare volume transport and eddy kinetic energy (EKE) in simulations with no trough or with enhanced horizontal

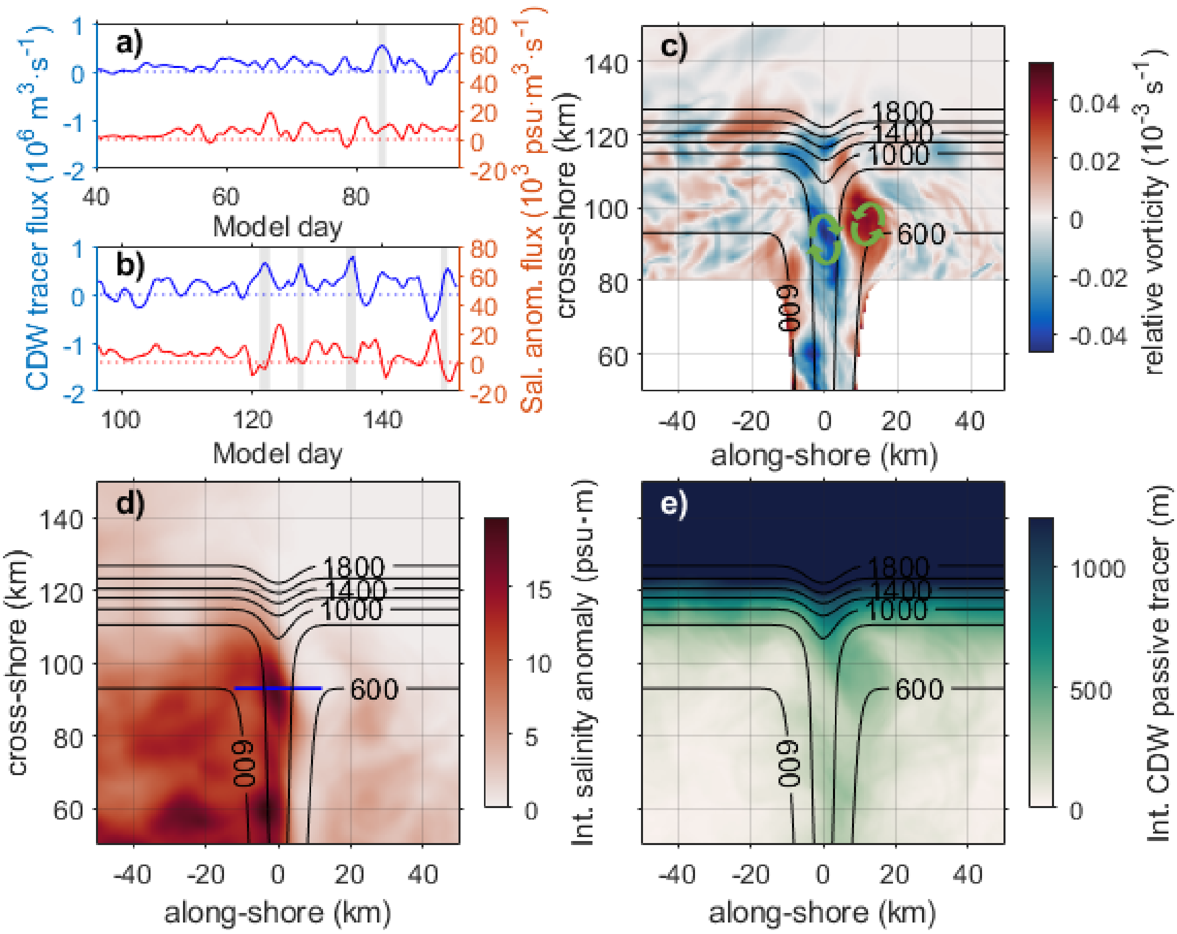

FIG. 10. (a-b) Time series of onshore flux of the CDW tracer (blue) and offshore flux of salinity anomaly (red) across the trough mouth (blue line in (d)), from Control Run 1. Time-averaged (c) relative vorticity at 580 m, (d) vertically-integrated salinity anomaly, and (e) vertically-integrated CDW tracer over periods of strong CDW onshore intrusion, as shaded gray in Panels (a) and (b). Green arrows in (c) indicate the mean flow pattern in the trough mouth region during the CDW intrusion periods.

viscosity to that of the control runs. In the no-trough simulation without resultant topographic steering, 4.4×10^{11} m^3 of DSW tracer reaches the deep sea offshore of the shelf break at Day 150, and 5.8×10^{10} m^3 of CDW tracer moves into the coastal region (within 25 km of the coast). These volumes are much smaller than the corresponding $22.1\times10^{11}\pm 1.9\times10^{11}$ m^3 of DSW tracer and $38.3\times10^{10}\pm 1.8\text{x}10^{10}$ m^3 of CDW tracer in the control runs. In the simulation with enhanced horizontal viscosity, DSW eddies are formed near the coast in the same way as in the control

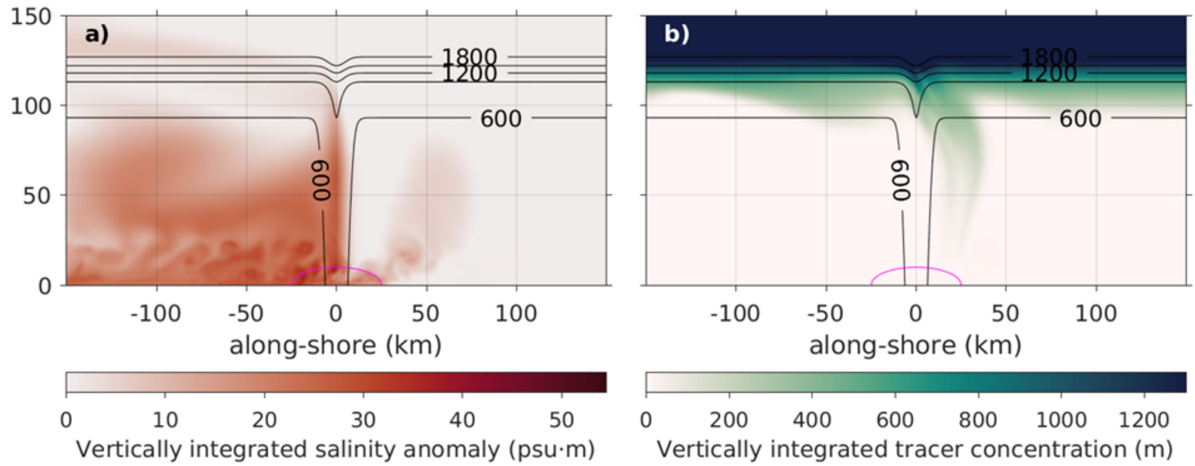

FIG. 11. Vertically integrated (a) salinity anomaly and (b) CDW tracer for a simulation with increased horizontal viscosity beyond 25 km offshore, at model Day 150. Black contours denote isobath contours. Magenta half-ellipse shows the region of surface buoyancy forcing.

runs, but they are suppressed by the large horizontal viscosity once they leave the coastal region. Consequently, the dense water outflow in the trough becomes nearly laminar (Fig. 11a). At Day 150, a small amount of CDW intrudes over the eastern continental shelf but not in the trough, and almost no CDW has reached the coastal region (Fig. 11b). This differs from the eddy-filled dense water outflow and coast-reaching CDW intrusion in the trough in the control runs (Fig. 2). With increased horizontal viscosity, EKE in the trough region averaged over days 80-150 decreases from $3.6\times10^{-3}\pm 0.4\times10^{-3}$ m^{2}s^{-2} in the control runs to 1.1×10^{-3} m^{2}s^{-2}; the volume of DSW reaching the deep sea at Day 150 reduces to 6.6×10^{11} m^3, and the volume of CDW reaching 25 km of the coast at Day 150 declines to 1.2×10^{10} m^3. Decreasing EKE clearly diminishes cross-shelf transport, due to both increased model spin up time and decreased equilibrium cross-shelf fluxes. These simulations confirm that both dense water eddies and topographic steering of these eddies by the trough enhance DSW eddy-driven CDW intrusions.

This eddy-driven, episodic onshore flow into the trough can be viewed, when averaged in time, as a geostrophic onshore current over the eastern half of the trough. The episodic sea level depression and elevation associated with the respective individual cyclonic and anticyclonic eddies in the trough (Fig. 7c-d, Fig. 10c), when averaged over time, form a positive along-shelf (cross-trough) sea level gradient over the eastern half of the trough (Fig. 4a). Associated with this temporal mean sea level gradient is a mean geostrophic onshore barotropic flow resulting from the time average of the individual submesoscale intrusion filaments (Fig. 4b). The averaged onshore flow appears similar to the intrusion process in Morrison et al. (2020). Thus, the intruding CDW filaments driven by mesoscale DSW eddies are a submesoscale process that, when averaged over time, manifests as the form stress mechanism described in Morrison et al. (2020). Note that the eddy-induced intrusion process described here not only provides a new submesoscale understanding of the intrusion dynamics of CDW at the trough mouth but also explains the continuous intrusion of CDW across the entire shelf toward the coast.

c. Impact of stratification

The control and sensitivity simulations discussed in the preceding sections have an unstratified ambient water column as an initial condition. However, at the onset of the austral winter, when sea ice and dense water start to form, the continental shelves surrounding Antarctica are often stratified (i.e. Gordon et al. 2000). To investigate the influence of water column stratification on the cross-shelf water exchange, we run simulations with varying initial stratification. In these simulations, the initial salinity increases linearly with depth at rates ranging from 0.03-0.5 psu km^{-1}. These salinity gradients are consistent with observations taken in the Antarctic coastal regions during the austral fall (Gordon et al. 2000; Williams et al. 2011; Ackley et al. 2020). Overall, the model results suggest that water column stratification suppresses cross-shelf water exchange at the trough mouth.

In unstratified simulations, DSW eddies fill the western half of the trough and flow offshore along the bottom (Fig. 12a). Adding stratification changes the dense water outflow to an intrusion at the level of neutral density. At an initial stratification of 0.2 psu km^{-1}, the core of the offshore spreading polynya-sourced water is raised to the depth of the trough rim (Fig 12b). The descending dense water spreads offshore along the trough rim at a speed of 1.9 ± 0.7 cm s^{-1}, much slower than the speed of 5.5 ± 1.0 cm s^{-1} in the control runs. When the initial stratification increases to 0.5 psu km^{-1}, the dense water formed at the polynya intrudes at mid-depth, above the trough rim (Fig. 12c), and its offshore velocity is an even slower 1.2 ± 0.7 cm s^{-1}. The neutral depth at which the dense water spreads offshore is determined by the initial stratification and factors that influence the density anomaly of the polynya-sourced water – i.e., surface buoyancy flux, Q, width of buoyancy

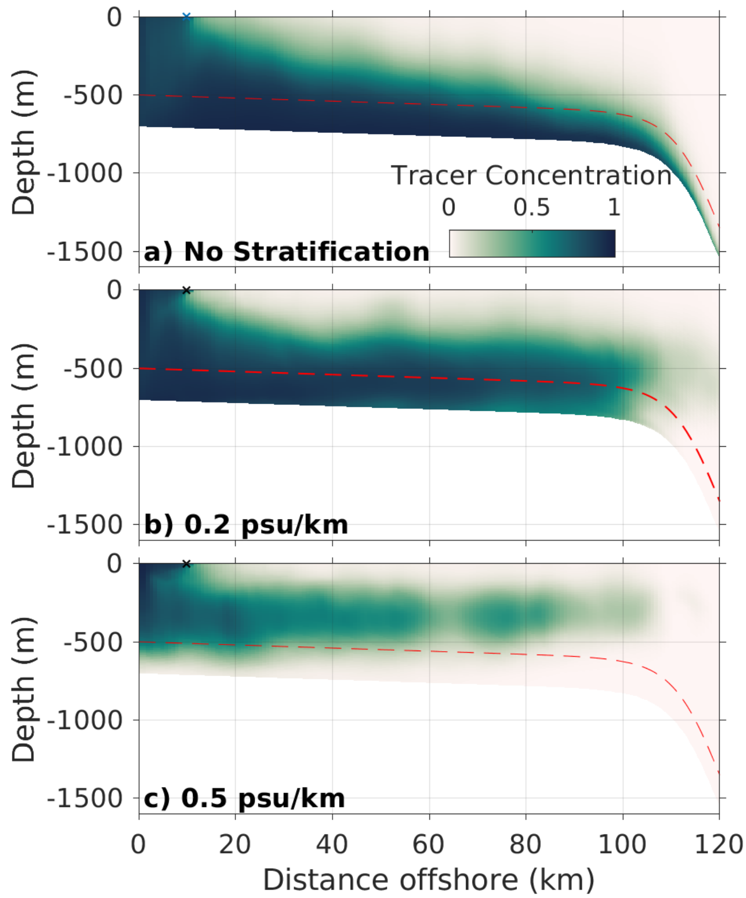

FIG. 12. Polynya-sourced passive tracer concentration along a transect taken 4 km west of the trough center (dashed line in Fig. 2b), averaged from days 100 to 150, for simulations with (a) no initial stratification (black solid circle in Fig. 14), (b) an initial stratification of 0.2 psu km^{-1} (black solid upper triangle in Fig. 14), and (c) an initial stratification of 0.5 psu km^{-1} (open diamond in Figure 14). The red dashed line indicates the depth of the trough rim. The black cross on the top of each panel denotes the furthermost offshore extent of the surface buoyancy forcing.

forcing region, b, and water column mixing. The effect of these factors on the dense water outflow in an unstratified water column are discussed in section 4a.

As the neutral depth of the polynya-sourced outflow rises in the water column, the influence of the topographic guide provided by the trough on the outflow diminishes. As the polynya-sourced water is at a neutral depth above the trough in the middle of the water column, there is no gravity force pulling it down the trough wall. No longer balanced between a down-slope pressure gradient

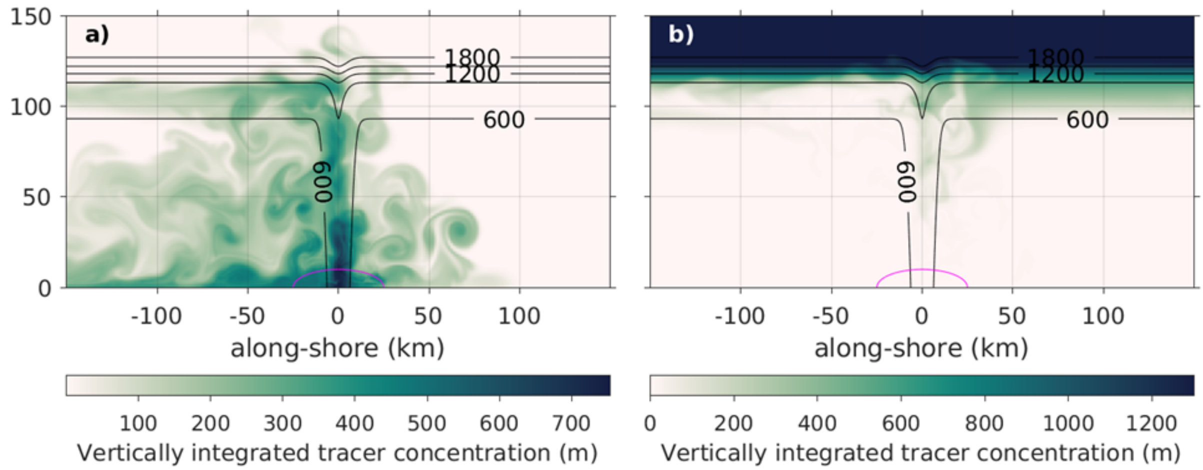

FIG. 13. Vertically integrated (a) dense water and (b) CDW tracer concentrations for a simulation with an initial stratification of 0.2 psu km^{-1}, at model day 150. Black contours denote isobath contours. Magenta half-ellipse shows the region of surface buoyancy forcing.

and up-slope Coriolis force, the water stops flowing offshore along the isobaths in the trough. Instead, eddy instabilities develop on the edge of the polynya-sourced water and gradually advect offshore at a much slower rate. Correspondingly, the simulation with the initial stratification of 0.2 psu km^{-1} has fewer eddies, and the eddies are more scattered over the continental shelf with no clear propagation pattern (Fig. 7e, f). Compared to Control Run 1 (Fig. 2e-f), dense water in the simulation with an initial stratification of 0.2 psu km^{-1} does not flow far offshore of the shelf break (Fig. 13a), and little CDW enters the continental shelf (Fig. 13b). This result is also consistent with simulations of different initial stratification showing that both integrated EKE in the trough and the amount of polynya-sourced passive tracer reaching offshore of the shelf break on Day 150 decrease with intensifying stratification (Fig. 14a, c).

Simulations with different initial stratification also show that increased stratification reduces the amount of CDW brought within 25 km of the coast (Fig. 14b). When the initial vertical salinity gradient is less than 0.1 psu km^{-1}, offshore transport of dense water and onshore transport of CDW are positively correlated, and the amount of CDW that intrudes close to the coast also correlates linearly with EKE inside the trough (Fig. 14d). This is a confirmation of the essential role of the offshore-moving dense water eddies in driving the CDW onshore intrusion. The dependence of

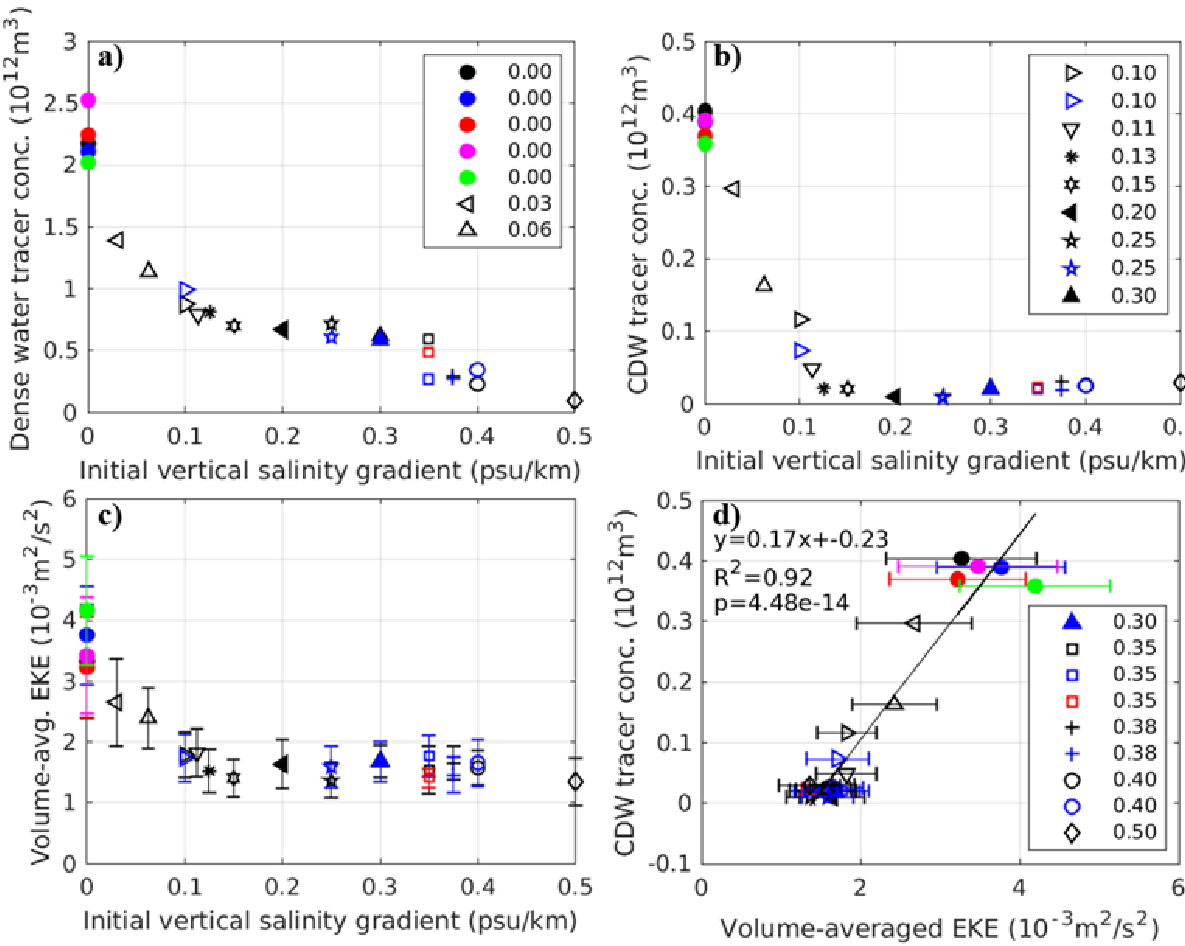

FIG. 14. Water mass transport in simulations with varying initial stratification. The top two panels show the total volume-integrated concentrations of (a) polynya-sourced dense water offshore of shelf break and b) CDW within 25km of the shore at Day 150 versus initial stratification. Panel (c) shows the volume-averaged EKE in the trough, averaged over days 80-150, versus initial stratification. Panel (d) shows the same CDW as in (b), now versus the volume- and time-averaged EKE at the trough. The legend, split between Panels (a), (b), and (d), labels simulations by initial vertical salinity gradient (psu km^{-1}). The error bars in (c-d) indicate one standard deviation in the volume-averaged EKE.

the CDW volume brought onto the entire continental shelf (inshore of the 600-m isobath) on initial stratification (not shown) is qualitatively similar to the pattern in Fig. 14b. This is consistent with the diminished topographic guide by the trough and less efficient onshore transport of CDW by disorganized eddies in simulations with strong initial stratification.

There are two possible mechanisms whereby increasing stratification diminishes onshore CDW intrusions. First, increasing salinity at depth reduces the density difference between the polynya-sourced dense water and the subsurface ambient waters on the shelf, limiting dense water formation and thereby reducing the potential energy available to be converted into EKE. Less EKE in the system means weaker dense water eddies and, thus, less entrainment of CDW onshore toward the coast. This mechanism is consistent with the conditions on warm Antarctic continental shelves, such as the Amundsen or Bellingshausen seas, which have strong stratification caused by CDW intrusions and surface meltwater influx. In the Amundsen Sea, observations show an absence of DSW (Narayanan et al. 2019), despite polynyas in the Amundsen Sea having high rates of sea ice production (Nihashi et al. 2017). Second, increasing initial stratification raises the neutral depth of the polynya-sourced dense water in the water column and makes the trough less effective at channeling dense water eddies. As the eddies start to become more disorganized and behave closer to those in the simulation without a trough (Fig. 7e-f), they stop working in unison to pull CDW shoreward along the trough. Instead, the eddies advect and disperse CDW over the continental shelf. The time-averaged onshore barotropic flow on the eastern slope of the trough ceases to exist, and CDW loses an efficient intrusion pathway. Essentially, adding stratification reduces CDW intrusions by reducing both EKE and the effectiveness of topographic steering.

5. Discussion

Our numerical simulations show that a trough aids buoyancy-driven cross-shelf exchange by lining up offshore-moving dense water eddies that entrain CDW onshore in a bucket brigade pattern. The limitations, applications, and implications of this mechanism are discussed below.

a. Limitations and future directions

Many significant processes known to drive circulation on the Antarctic continental shelf are neglected here, and their influence on the exchange process identified here is untested. For instance, CDW intrusions can be driven by surface wind stress (Thoma et al. 2008), sea ice stress (Kim et al. 2017), ice shelf melt (St-Laurent et al. 2013), tidal rectification (Wang et al. 2013), and shelf break currents (St-Laurent et al. 2013). Such processes may obscure the signal of cross-shelf exchange caused by dense water eddies in the ocean. For instance, lateral export of dense water from the polynya driven by surface winds (Xu et al. in revision) or a coastal current (Chapman 2000) decreases the residence time of dense water in the polynya, exposing the water parcel to less brine rejection and thereby reducing the buoyancy anomaly of the polynya-sourced dense water relative to ambient waters. This reduced buoyancy anomaly likely weakens the dense water eddies in the trough and thus reduces buoyancy driven cross-shelf exchange. Similarly, tidal mixing of dense and ambient waters can suppress exchange (Bowen et al. 2021), as could mixing induced by other processes, such as shelf-break mixing. Additionally, the model does not include an Antarctic Slope Front, which acts to limit cross-slope transport (Goddard et al. 2017), although instabilities in the Antarctic Slope Current (ASC) and interactions with the ASC and a trough can enhance CDW intrusions (Zhang et al. 2011; St-Laurent et al. 2013). Meanwhile, stratification limits polynya dense water formation (Snow et al. 2016; Aoki et al. 2022) and reduces the buoyancy-driven cross-shelf exchange in an idealized case (section 4c). A more realistic pycnocline structure could modify how much topographic steering a trough exerts on DSW eddies. Furthermore, in the unstratified control runs, the inflow of CDW is barotropic, so surface waters also intrude shoreward; the vertical structure of shoreward intrusions with realistic stratification profiles warrants further study.

The surface buoyancy forcing, Q, and vertical mixing scheme used in this study affects the magnitude and density of DSW formed, with implications for the DSW current speed (due to the reduced gravity term in Equation 4) and strength of CDW intrusions. However, the underlying dynamical mechanism linking dense water formation to eddy-driven CDW intrusions is not expected to depend on Q nor the vertical mixing scheme. Indeed, while a sensitivity simulation with reduced Q results in less DSW offshore flux, less EKE, and less CDW intrusions than in the control runs, eddies still exist in the trough and pull CDW onshore (not shown).

This study uses an idealized trough geometry, while troughs on the Antarctic shelf are much more complex with varying orientations, lengths, widths, slopes (retrograde or prograde), alongshore location relative to polynyas, and along-trough bathymetric heterogeneity such as sills. We expect that both a trough located further from a polynya and a longer trough would result in a more diluted DSW current. A narrower trough with steeper side walls makes DSW flow faster (Equation 6), but at some critical width smaller than the baroclinic deformation radius a trough will be too narrow to fit DSW eddies. Conversely, wide troughs could channel more DSW offshore, but could also have less confined eddy pathways. Finally, along-trough bathymetric heterogeneity could increase mixing of DSW with ambient waters, thereby weakening the DSW outflow and CDW inflow. More research is needed to determine how DSW and CDW transport depends on differing trough geometries.

The cross-shelf exchange process identified in this study requires dense water to form near the head of a prograde trough with a width of a similar scale as the eddy diameter, i.e., a few times larger than the deformation radius. A few troughs around Antarctica satisfy this criterion, including two prograde troughs off Enderby Land (Fig. 1d) within 225 km of an observed DSW cascade (Amblas and Dowdeswell 2018) and a prograde trough offshore of Oates Land (157°E, 68.85°S) adjacent to an inferred DSW cascade (Amblas and Dowdeswell 2018). Due to a lack of observations, it is unknown if CDW intrusions occur in these troughs. Observing flows in this type of prograde troughs is thus a logical future direction for a complete understanding of cross-shelf exchange processes at the Antarctic shelf edge. However, as retrograde troughs are more common around Antarctica, another future direction should be to examine submesoscale processes of cross-shelf-edge exchange and onshore intrusion of CDW in retrograde troughs all the way from the shelf break to the polynya region, particularly in known regions of CDW intrusions such as the Drygalski Trough, Adélie Depression, and Filchner Trough (Castagno et al. 2017; Martin et al. 2017; Ryan et al. 2020). Note that the eddy process identified here might not be applicable in retrograde troughs as the rising seafloor of retrograde troughs toward the shelf edge presumably suppresses vortex vertical stretching, hinders DSW eddy formation, and thus reduces eddy impact on CDW intrusions.

b. Application in the ocean

Despite these idealized simplifications, the model simulations produce cyclonic dense water eddies that match observations from Antarctic troughs. A rotary current spectra of velocity at the trough mouth over days 80 to 150 is computed using Slepian tapers with a time-bandwidth product of 4 (Fig. 15). The modelled cyclonic eddies drive variability in near-bottom velocities in the trough at a dominant period of 3 to 4 days. This timescale is consistent with observed variability along the continental slope of the Weddell Sea (Daae et al. 2019; Jensen et al. 2013), which Daae et al. (2019) posit to be caused by westward-propagating topographic vorticity waves or dense water eddies that form due to vortex stretching (Daae et al. 2019; Lane-Serff and Baines 2000).

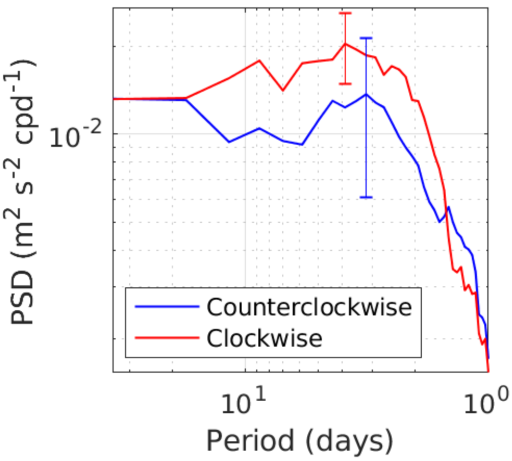

FIG. 15. Rotary spectra of current velocity at a virtual mooring located in the trough mouth at the shelf break (red diamond in Fig. 2b) at 10 m above the bottom, averaged between the five control runs. Error bars show the standard deviation at peak frequencies.

This agreement in modelled and observed peaks in variability, while not conclusive, suggests that the modelled cyclonic eddies occur in Antarctic troughs. Furthermore, observations in a trough show that peaks in offshore flow at one location correlate with onshore flow at another location to its east (Darelius et al. 2023), suggesting that dense water cyclonic eddies correlate in time with episodic large onshore CDW volume fluxes. Furthermore, the modeled main pathway of onshore intrusions is on the eastern side of the trough, which largely agrees with observations showing warm water intrusions in the eastern flanks of Antarctic troughs in areas of DSW formation (Kohut et al. 2013; Castagno et al. 2017; Martin et al. 2017; Ryan et al. 2020; Ribeiro et al. 2021).

The modelled volume flux of CDW onto the continental shelf is comparable to previous estimates. Using a realistic pan-Antarctic ocean model with a 2.6 to 5.5 km horizontal resolution, Morrison et al. (2020) estimated that 0.5 to 1 Sv per 100 km of CDW is carried onto the continental shelf by the mean onshore flow in each of the troughs in the Ross Sea. Interestingly, in the control simulations of this study, which has a higher resolution and a narrower trough, the eddy-driven, episodic onshore flow in the trough carries about 0.3 Sv of CDW passive tracer onto the shelf onshore of the 600 m isobath over the first 150 days. This transport occurs across roughly a 150 km long section of the shelf break (Fig. 2f). That is, our model simulations provide an estimate of the cross-shelf CDW volume fluxes of a similar order of magnitude as Morrison et al. (2020), despite the difference in transport mechanisms. Thus, the dense shelf water outflow simulated in this study has the potential to drive a significant portion of the onshore transport of CDW.

c. Implications

Eddy-driven CDW intrusions could impact the regional climate. Firstly, as a mechanism for bringing warm CDW across the shelf towards the coast, this process can contribute to the melting of sea ice and ice shelves. However, stronger water-column stratification suppresses this type of CDW intrusion by weakening DSW formation and EKE on the shelf (section 4c). Thus, as the ocean warms and dense water formation slows (Lago and England 2019), this CDW intrusion mechanism may occur less frequently. As a result, a negative feedback loop is possible wherein increased surface meltwater increases stratification and decreases CDW onshore intrusions, resulting in less heat available to melt ice. Meanwhile, this negative feedback loop acts opposite to and potentially balances a positive feedback loop. In the positive loop, stratification inhibits winter convection (Silvano et al. 2017) and allows CDW to reside at depth on the shelf for longer instead of being mixed up to the surface layer and losing its heat to the atmosphere (Narayanan et al. 2019). This positive feedback means more heat from offshore could reach and melt ice shelves (Dutrieux et al. 2014). The relationship between these two opposing feedbacks should be examined further.

Numerical models must resolve or parameterize these eddy-driven CDW intrusions to simulate their potential impacts on the climate system. Eddies greatly enhance the cross-shelf exchange of DSW and CDW, as demonstrated by comparing a simulation with enhanced horizontal viscosity (Fig. 11) to a control simulation (Fig. 2). As discussed in section 4c, this enhanced horizontal viscosity lowers the average EKE in the trough, decreases the offshore flux of DSW, and decreases the onshore flux of CDW. Reducing the model grid resolution is expected to have a similar impact as enhancing horizontal viscosity in this study and, thus, reduce cross-shelf exchange. Current climate models have resolutions on the order of a degree, which is roughly ten times larger than the first baroclinic Rossby radius of deformation along the Antarctic slope. As such, these models cannot resolve mesoscale DSW eddies and likely underestimate the strength of CDW intrusions in regions of the Antarctic continental shelf where this eddy-driven exchange is active.

6. Summary

This study investigates the flow of dense water, formed in an Antarctic coastal polynya, down a trough and identifies a new process for onshore CDW intrusions. Numerical simulations show that the dense water flows along the bottom of the trough as an eddy-dominated bottom gravity current. Comparison with an analytical scaling finds that this current is driven by a cross-trough baroclinic pressure gradient balanced by the Coriolis force, has an along-trough velocity proportional to the reduced gravity of the dense water and the slope of the trough side wall, and inversely proportional to the Coriolis parameter. The trough is shown to topographically guide cyclonic dense-water eddies into a consistent pathway from the coast to the shelf break, forming an eddy chain residing in the trough at any given time. This consistent chain of offshore-moving eddies then works together to entrain CDW from offshore, first across the shelf edge into the trough and, then, along the trough towards the coast, in a pattern similar to a fire bucket brigade passing water buckets toward a fire. This eddy mechanism transports relatively warm CDW to the Antarctic coastal region, where the imported heat could melt sea ice and ice shelves.

The process of onshore CDW intrusion identified in this study requires dense shelf water formation near the head of a cross-shelf oriented, prograde trough – a condition that is met in a few regions of the Antarctic coast. It implies that substantial water exchange between the Antarctic continental shelf and the deep ocean could occur in shelf edge regions with irregular topography. This is consistent with results of observational and numerical studies around Antarctica. The CDW onshore flux estimated in our idealized models is of the same order of magnitude as those estimated in a previous realistic simulation. As the idealized configuration employed here neglects the influence of multiple factors that could substantially impact the circulation on the Antarctic shelf, the exact contribution of the eddy-driven transport mechanism identified here on the overall water exchange between the Antarctic shelf and the deep water remains to be explored in future observational or modeling studies.

Acknowledgments. Thanks Phadtaya Poemnamthip and Yilang Xu for assistance setting up the numerical models. This study was supported by National Science Foundation through grants OCE-2147884 and OPP-1643901. The authors declare that they have no conflicting interests.

Data availability statement. The ROMS configuration files and Matlab scripts used to generate input files for the numerical simulations are available at: https://doi.org/10.5281/zenodo.7964037

References

Ackley, S. F., and Coauthors, 2020: Sea-ice production and air/ice/ocean/biogeochemistry interactions in the Ross Sea during the PIPERS 2017 autumn field campaign. *Annals of Glaciology*, **61 (82)**, 181–195, https://doi.org/10.1017/aog.2020.31.

Amblas, D., and J. A. Dowdeswell, 2018: Physiographic influences on dense shelf-water cascading down the Antarctic continental slope. *Earth-Science Reviews*, **185**, 887–900, https://doi.org/10.1016/j.earscirev.2018.07.014.

Aoki, S., T. Takahashi, K. Yamazaki, D. Hirano, K. Ono, K. Kusahara, T. Tamura, and G. D. Williams, 2022: Warm surface waters increase Antarctic ice shelf melt and delay dense water formation. *Communications Earth & Environment*, **3 (1)**, 1–8, https://doi.org/10.1038/s43247-022-00456-z.

Bowen, M. M., D. Fernandez, A. Forcen-Vazquez, A. L. Gordon, B. Huber, P. Castagno, and P. Falco, 2021: The role of tides in bottom water export from the western Ross Sea. *Scientific Reports*, **11 (1)**, 2246, https://doi.org/10.1038/s41598-021-81793-5.

Castagno, P., P. Falco, M. S. Dinniman, G. Spezie, and G. Budillon, 2017: Temporal variability of the Circumpolar Deep Water inflow onto the Ross Sea continental shelf. *Journal of Marine Systems*, **166**, 37–49, https://doi.org/10.1016/j.jmarsys.2016.05.006.

Cenedese, C., J. A. Whitehead, T. A. Ascarelli, and M. Ohiwa, 2004: A Dense Current Flowing down a Sloping Bottom in a Rotating Fluid. *Journal of Physical Oceanography*, **34 (1)**, 188–203, https://doi.org/10.1175/1520-0485(2004)034⟨0188:ADCFDA⟩2.0.CO;2.

Chapman, D. C., 1985: Numerical Treatment of Cross-Shelf Open Boundaries in a Barotropic Coastal Ocean Model. *Journal of Physical Oceanography*, **15 (8)**, 1060–1075, https://doi.org/10.1175/1520-0485(1985)015⟨1060:NTOCSO⟩2.0.CO;2.

Chapman, D. C., 1999: Dense Water Formation beneath a Time-Dependent Coastal Polynya. *Journal of Physical Oceanography*, **29 (4)**, 807–820, https://doi.org/10.1175/1520-0485(1999)029⟨0807:DWFBAT⟩2.0.CO;2.

Chapman, D. C., 2000: The influence of an alongshelf current on the formation and offshore transport of dense water from a coastal polynya. *Journal of Geophysical Research: Oceans*, **105 (C10)**, 24 007–24 019, https://doi.org/10.1029/2000JC000296.

Chapman, D. C., and G. Gawarkiewicz, 1995: Offshore transport of dense shelf water in the presence of a submarine canyon. *Journal of Geophysical Research: Oceans*, **100 (C7)**, 13 373–13 387, https://doi.org/10.1029/95JC00890.

Chapman, D. C., and G. Gawarkiewicz, 1997: Shallow Convection and Buoyancy Equilibration in an Idealized Coastal Polynya. *Journal of Physical Oceanography*, **27 (4)**, 555–566, https://doi.org/10.1175/1520-0485(1997)027⟨0555:SCABEI⟩2.0.CO;2.

Cherian, D. A., and K. H. Brink, 2016: Offshore Transport of Shelf Water by Deep-Ocean Eddies. *Journal of Physical Oceanography*, **46 (12)**, 3599–3621, https://doi.org/10.1175/JPO-D-16-0085.1.

Daae, K., I. Fer, and E. Darelius, 2019: Variability and Mixing of the Filchner Overflow Plume on the Continental Slope, Weddell Sea. *Journal of Physical Oceanography*, **49 (1)**, 3–20, https://doi.org/10.1175/JPO-D-18-0093.1.

Darelius, E., and Coauthors, 2023: Observational evidence for on-shelf heat transport driven by dense water export in the Weddell Sea. *Nature Communications*, **14 (1)**, 1022, https://doi.org/10.1038/s41467-023-36580-3.

Dinniman, M. S., J. M. Klinck, and W. O. Smith, 2003: Cross-shelf exchange in a model of the Ross Sea circulation and biogeochemistry. *Deep Sea Research Part II: Topical Studies in Oceanography*, **50 (22)**, 3103–3120, https://doi.org/10.1016/j.dsr2.2003.07.011.

Dutrieux, P., and Coauthors, 2014: Strong Sensitivity of Pine Island Ice-Shelf Melting to Climatic Variability. *Science*, **343 (6167)**, 174–178, https://doi.org/10.1126/science.1244341.

Faghmous, J. H., I. Frenger, Y. Yao, R. Warmka, A. Lindell, and V. Kumar, 2015: A daily global mesoscale ocean eddy dataset from satellite altimetry. *Scientific Data*, **2 (1)**, 150 028, https://doi.org/10.1038/sdata.2015.28.

Garfield III, N., and D. L. Evans, 1987: Shelf water entrainment by Gulf Stream warm-core rings. *Journal of Geophysical Research: Oceans*, **92 (C12)**, 13 003–13 012, https://doi.org/10.1029/JC092iC12p13003.

Gawarkiewicz, G., 2000: Effects of ambient stratification and shelfbreak topography on offshore transport of dense water on continental shelves. *Journal of Geophysical Research: Oceans*, **105 (C2)**, 3307–3324, https://doi.org/10.1029/1999JC900298.

Gawarkiewicz, G., and D. C. Chapman, 1995: A numerical study of dense water formation and transport on a shallow, sloping continental shelf. *Journal of Geophysical Research: Oceans*, **100 (C3)**, 4489–4507, https://doi.org/10.1029/94JC01742.

Goddard, P. B., C. O. Dufour, J. Yin, S. M. Griffies, and M. Winton, 2017: CO2-Induced Ocean Warming of the Antarctic Continental Shelf in an Eddying Global Climate Model. *Journal of Geophysical Research: Oceans*, **122 (10)**, 8079–8101, https://doi.org/10.1002/2017JC012849.

Gordon, A. L., A. H. Orsi, R. Muench, B. A. Huber, E. Zambianchi, and M. Visbeck, 2009: Western Ross Sea continental slope gravity currents. *Deep Sea Research Part II: Topical Studies in Oceanography*, **56 (13)**, 796–817, https://doi.org/10.1016/j.dsr2.2008.10.037.

Gordon, L. I., L. A. Codispoti, J. C. Jennings, F. J. Millero, J. M. Morrison, and C. Sweeney, 2000: Seasonal evolution of hydrographic properties in the Ross Sea, Antarctica, 1996–1997. *Deep Sea Research Part II: Topical Studies in Oceanography*, **47 (15)**, 3095–3117, https://doi.org/10.1016/S0967-0645(00)00060-6.

Guo, G., J. Shi, L. Gao, T. Tamura, and G. D. Williams, 2019: Reduced Sea Ice Production Due to Upwelled Oceanic Heat Flux in Prydz Bay, East Antarctica. *Geophysical Research Letters*, **46 (9)**, 4782–4789, https://doi.org/10.1029/2018GL081463.

Haidvogel, D. B., and Coauthors, 2008: Ocean forecasting in terrain-following coordinates: Formulation and skill assessment of the Regional Ocean Modeling System. *Journal of Computational Physics*, **227 (7)**, 3595–3624, https://doi.org/10.1016/j.jcp.2007.06.016.

Jacobs, S. S., H. H. Hellmer, and A. Jenkins, 1996: Antarctic Ice Sheet melting in the southeast Pacific. *Geophysical Research Letters*, **23 (9)**, 957–960, https://doi.org/10.1029/96GL00723.

Jensen, M. F., I. Fer, and E. Darelius, 2013: Low frequency variability on the continental slope of the southern Weddell Sea. *Journal of Geophysical Research: Oceans*, **118 (9)**, 4256–4272, https://doi.org/10.1002/jgrc.20309.

Johnson, G. C., 2008: Quantifying Antarctic Bottom Water and North Atlantic Deep Water volumes. *Journal of Geophysical Research: Oceans*, **113 (C5)**, https://doi.org/10.1029/2007JC004477.

Kämpf, J., 2005: Cascading-driven upwelling in submarine canyons at high latitudes. *Journal of Geophysical Research: Oceans*, **110 (C2)**, https://doi.org/10.1029/2004JC002554.

Kim, T. W., H. K. Ha, A. K. Wåhlin, S. H. Lee, C. S. Kim, J. H. Lee, and Y. K. Cho, 2017: Is Ekman pumping responsible for the seasonal variation of warm circumpolar deep water in the Amundsen Sea? *Continental Shelf Research*, **132**, 38–48, https://doi.org/10.1016/j.csr.2016.09.005.

Klinck, J. M., and M. S. Dinniman, 2010: Exchange across the shelf break at high southern latitudes. *Ocean Science*, **6 (2)**, 513–524, https://doi.org/10.5194/os-6-513-2010.

Klinck, J. M., E. E. Hofmann, R. C. Beardsley, B. Salihoglu, and S. Howard, 2004: Water-mass properties and circulation on the west Antarctic Peninsula Continental Shelf in Austral Fall and Winter 2001. *Deep Sea Research Part II: Topical Studies in Oceanography*, **51 (17)**, 1925–1946, https://doi.org/10.1016/j.dsr2.2004.08.001.

Kohut, J., E. Hunter, and B. Huber, 2013: Small-scale variability of the cross-shelf flow over the outer shelf of the Ross Sea. *Journal of Geophysical Research: Oceans*, **118 (4)**, 1863–1876, https://doi.org/10.1002/jgrc.20090.

Lago, V., and M. H. England, 2019: Projected Slowdown of Antarctic Bottom Water Formation in Response to Amplified Meltwater Contributions. *Journal of Climate*, **32 (19)**, 6319–6335, https://doi.org/10.1175/JCLI-D-18-0622.1.

Lane-Serff, G. F., and P. G. Baines, 2000: Eddy Formation by Overflows in Stratified Water. *Journal of Physical Oceanography*, **30 (2)**, 327–337, https://doi.org/10.1175/1520-0485(2000)030⟨0327:EFBOIS⟩2.0.CO;2.

Liu, C., Z. Wang, X. Liang, X. Li, X. Li, C. Cheng, and D. Qi, 2022: Topography-Mediated Transport of Warm Deep Water across the Continental Shelf Slope, East Antarctica. *Journal of Physical Oceanography*, **52 (6)**, 1295–1314, https://doi.org/10.1175/JPO-D-22-0023.1.

Livingstone, S. J., C. Ó Cofaigh, C. R. Stokes, C.-D. Hillenbrand, A. Vieli, and S. S. R. Jamieson, 2012: Antarctic palaeo-ice streams. *Earth-Science Reviews*, **111 (1)**, 90–128, https://doi.org/10.1016/j.earscirev.2011.10.003.

Martin, A., M.-N. Houssais, H. Le Goff, C. Marec, and D. Dausse, 2017: Circulation and water mass transports on the East Antarctic shelf in the Mertz Glacier region. *Deep Sea Research Part I: Oceanographic Research Papers*, **126**, 1–20, https://doi.org/10.1016/j.dsr.2017.05.007.

Morrison, A. K., A. McC. Hogg, M. H. England, and P. Spence, 2020: Warm Circumpolar Deep Water transport toward Antarctica driven by local dense water export in canyons. *Science Advances*, **6 (18)**, eaav2516, https://doi.org/10.1126/sciadv.aav2516.

Narayanan, A., S. T. Gille, M. R. Mazloff, and K. Murali, 2019: Water Mass Characteristics of the Antarctic Margins and the Production and Seasonality of Dense Shelf Water. *Journal of Geophysical Research: Oceans*, **124 (12)**, 9277–9294, https://doi.org/10.1029/2018JC014907.

Nihashi, S., K. I. Ohshima, and T. Tamura, 2017: Sea-Ice Production in Antarctic Coastal Polynyas Estimated From AMSR2 Data and Its Validation Using AMSR-E and SSM/I-SSMIS Data. *IEEE Journal of Selected Topics in Applied Earth Observations and Remote Sensing*, **10 (9)**, 3912–3922, https://doi.org/10.1109/JSTARS.2017.2731995.

Nof, D., 1983: The translation of isolated cold eddies on a sloping bottom. *Deep Sea Research Part A. Oceanographic Research Papers*, **30 (2)**, 171–182, https://doi.org/10.1016/0198-0149(83)90067-5.

Orlanski, I., 1976: A simple boundary condition for unbounded hyperbolic flows. *Journal of Computational Physics*, **21 (3)**, 251–269, https://doi.org/10.1016/0021-9991(76)90023-1.

Ribeiro, N., L. Herraiz-Borreguero, S. R. Rintoul, C. R. McMahon, M. Hindell, R. Harcourt, and G. Williams, 2021: Warm Modified Circumpolar Deep Water Intrusions Drive Ice Shelf Melt and Inhibit Dense Shelf Water Formation in Vincennes Bay, East Antarctica. *Journal of Geophysical Research: Oceans*, **126 (8)**, e2020JC016 998, https://doi.org/10.1029/2020JC016998.

Ryan, S., H. H. Hellmer, M. Janout, E. Darelius, L. Vignes, and M. Schröder, 2020: Exceptionally Warm and Prolonged Flow of Warm Deep Water Toward the Filchner-Ronne Ice Shelf in 2017. *Geophysical Research Letters*, **47 (13)**, e2020GL088 119, https://doi.org/10.1029/2020GL088119.

Shchepetkin, A. F., and J. C. McWilliams, 2005: The regional oceanic modeling system (ROMS): A split-explicit, free-surface, topography-following-coordinate oceanic model. *Ocean Modelling*, **9 (4)**, 347–404, https://doi.org/10.1016/j.ocemod.2004.08.002.

Silvano, A., S. R. Rintoul, B. Peña-Molino, and G. D. Williams, 2017: Distribution of water masses and meltwater on the continental shelf near the Totten and Moscow University ice shelves. *Journal of Geophysical Research: Oceans*, **122 (3)**, 2050–2068, https://doi.org/10.1002/2016JC012115.

Snow, K., A. M. Hogg, B. M. Sloyan, and S. M. Downes, 2016: Sensitivity of Antarctic Bottom Water to Changes in Surface Buoyancy Fluxes. *Journal of Climate*, **29 (1)**, 313–330, https://doi.org/10.1175/JCLI-D-15-0467.1.

St-Laurent, P., J. M. Klinck, and M. S. Dinniman, 2013: On the Role of Coastal Troughs in the Circulation of Warm Circumpolar Deep Water on Antarctic Shelves. *Journal of Physical Oceanography*, **43 (1)**, 51–64, https://doi.org/10.1175/JPO-D-11-0237.1.

Stewart, A. L., A. Klocker, and D. Menemenlis, 2018: Circum-Antarctic Shoreward Heat Transport Derived From an Eddy- and Tide-Resolving Simulation. *Geophysical Research Letters*, **45 (2)**, 834–845, https://doi.org/10.1002/2017GL075677.

Swaters, G. E., 1998: Numerical simulations of the baroclinic dynamics of density-driven coupled fronts and eddies on a sloping bottom. *Journal of Geophysical Research: Oceans*, **103 (C2)**, 2945–2961, https://doi.org/10.1029/97JC02441.

Thoma, M., A. Jenkins, D. Holland, and S. Jacobs, 2008: Modelling Circumpolar Deep Water intrusions on the Amundsen Sea continental shelf, Antarctica. *Geophysical Research Letters*, **35 (18)**, https://doi.org/10.1029/2008GL034939.

Wåhlin, A. K., 2004: Downward channeling of dense water in topographic corrugations. *Deep Sea Research Part I: Oceanographic Research Papers*, **51 (4)**, 577–590, https://doi.org/10.1016/j.dsr.2003.11.002.

Walker, D. P., M. A. Brandon, A. Jenkins, J. T. Allen, J. A. Dowdeswell, and J. Evans, 2007: Oceanic heat transport onto the Amundsen Sea shelf through a submarine glacial trough. *Geophysical Research Letters*, **34 (2)**, https://doi.org/10.1029/2006GL028154.

Wang, Q., S. Danilov, H. Hellmer, D. Sidorenko, J. Schröter, and T. Jung, 2013: Enhanced cross-shelf exchange by tides in the western Ross Sea. *Geophysical Research Letters*, **40 (21)**, 5735–5739, https://doi.org/10.1002/2013GL058207.

Williams, G. D., M. Hindell, M.-N. Houssais, T. Tamura, and I. C. Field, 2011: Upper ocean stratification and sea ice growth rates during the summer-fall transition, as revealed by Elephant seal foraging in the Adélie Depression, East Antarctica. *Ocean Science*, **7 (2)**, 185–202, https://doi.org/10.5194/os-7-185-2011.

Xu, Y., W. G. Zhang, T. Maksym, R. Ji, and Y. Li, in revision: Stratification breakdown in Antarctic coastal polynyas, Part I: Influence of physical factors on the destratification timescale. *Journal of Physical Oceanography*.

Zhang, W. G., and C. Cenedese, 2014: The Dispersal of Dense Water Formed in an Idealized Coastal Polynya on a Shallow Sloping Shelf. *Journal of Physical Oceanography*, **44 (6)**, 1563–1581, https://doi.org/10.1175/JPO-D-13-0188.1.

Zhang, W. G., and S. J. Lentz, 2017: Wind-Driven Circulation in a Shelf Valley. Part I: Mechanism of the Asymmetrical Response to Along-Shelf Winds in Opposite Directions. *Journal of Physical Oceanography*, **47 (12)**, 2927–2947, https://doi.org/10.1175/JPO-D-17-0083.1.

Zhang, W. G., and Coauthors, 2023: Cross-shelf exchange associated with a shelf-water streamer at the Mid-Atlantic Bight shelf edge. *Progress in Oceanography*, **210**, 102 931, https://doi.org/10.1016/j.pocean.2022.102931.

Zhang, Y., J. Pedlosky, and G. R. Flierl, 2011: Shelf Circulation and Cross-Shelf Transport out of a Bay Driven by Eddies from an Open-Ocean Current. Part I: Interaction between a Barotropic Vortex and a Steplike Topography. *Journal of Physical Oceanography*, **41 (5)**, 889–910, https://doi.org/10.1175/2010JPO4496.1.